International Journal of Solids and Structures 279 (2023) 112344

Contents lists available at ScienceDirect

International Journal of Solids and Structures

journal homepage: www.elsevier.com/locate/ijsolstr

A mechanics model of hard-magnetic soft rod with deformable cross-section under three-dimensional large deformation

Xin Li [a], Wenkai Yu [a], Jingyi Liu [a], Xiaoyan Zhu [a], Huiru Wang [a], Xiaoyu Sun [b], Ju Liu [a], Hongyan Yuan [a,*]

[a] Shenzhen Key Laboratory of Soft Mechanics & Smart Manufacturing, Department of Mechanics and Aerospace Engineering, Southern University of Science and Technology, Shenzhen 518055, China
[b] PengCheng Laboratory, Shenzhen 518055, China

ARTICLE INFO

Keywords:
Hard-magnetic soft (HMS) rod
Deformable cross-section
Non-Hookean materials
3D large deformation
Magnetic field

ABSTRACT

Hard-magnetic soft (HMS) materials are soft active materials prepared by embedding the hard-magnetic particles (e.g. NdFeB) into soft elastomer, which can be actuated by applied magnetic fields. With the ability to retain remnant magnetism, HMS materials have many applications in soft robotics, haptic sensors and other fields. For HMS structures used in soft robotics, mechanics models have been developed for better exploiting the potential of the HMS materials. However, for rod-like structures made of soft materials, the nonlinear stress–strain relation and the areal change of the cross-section have not been considered in previous modeling work. In the present three-dimensional HMS rod model, started with the geometrically exact beam theory, the rigid cross-section assumption is replaced with a planar areal change assumption for soft rods, incompressible neo-Hookean material model is used to model the hyperelastic behavior of elastomers, which will be more accurate than linear relation under large deformation. Consistent with the deformable cross-section assumption, the magneto-elastic energy distribution is formulated and reduced to the line of centroid of the soft rod. To verify the accuracy and efficiency of the model, some simulation examples and experiments are performed. The error between the experimental results and the simulation results calculated by using 5 elements is within 10%. Our model can accurately and efficiently predict the 3D large deformation of the HMS rod, which can reduce the design and optimization cost and shorten the design cycle of HMS structure.

1. Introduction

Due to their low elastic modulus, soft active materials usually possess the ability to achieve rapid and large deformation through various external stimuli such as variable length tendons (Yu et al., 2022), pressure differential (Ma and Zhou, 2023), temperature (Kang et al., 2019), light (Chen et al., 2021), electric (Cao et al., 2019) and magnetic fields (Kim et al., 2018; Du et al., 2020), making them exhibit great potential in the fields of biomedical engineering (Joo et al., 2021), soft robotics (Ye et al., 2022) and mechanical sensors (Yu et al., 2022), etc. Compared to other stimuli mechanisms, magnetic fields have unique merits: (1) magnetic actuation performs well in the enclosed space, due to the high penetration ability of magnetic fields into a wide range of materials (Hines et al., 2017; Sitti and Wiersma, 2020; Chung et al., 2021); (2) the response time of magnetic actuation is relatively short (Chung et al., 2021). Therefore, magnetoactive soft materials have been extensively studied over the last few decades.

In recent years, a new class of magnetoactive soft materials has attracted the interest from researchers, viz, hard-magnetic soft (HMS) materials. HMS materials are fabricated by incorporating hard-magnetic particles, such as NdFeB magnets, into soft polymers, and the material has been realized in a series of soft matrices (Wang et al., 2004; Stepanov et al., 2012; Furusawa et al., 2019). A number of HMS robots have been developed in the past, to mention only a few examples, a shape-programmable HMS robot (Lum et al., 2016), a millimeter-scale HMS swimming robot (Diller et al., 2014), and a small-scale soft continuous robot with active steering and navigation presented (Kim et al., 2019). In addition, the fabrication schemes of HMS robots have made significant progress. A series of additive manufacturing methods, such as 3D printing (Kim et al., 2018; Xu et al., 2019), are adopted.

Benefiting from the large magnetic hysteresis with the high coercivity and high remanence of the HMS materials, programmable and complex deformations of magnetic driven robot becomes possible (Kim

* Corresponding author.
E-mail address: yuanhy3@sustech.edu.cn (H. Yuan).

https://doi.org/10.1016/j.ijsolstr.2023.112344
Received 4 February 2023; Received in revised form 10 May 2023; Accepted 24 May 2023
Available online 29 May 2023

Nomenclature

L, S initial total length of the rod, arc length of the line of centroids in the reference configuration
τ time
$\vec{e}_1$, $\vec{e}_2$, $\vec{e}_3$ basis of the fixed Cartesian coordinate system
$\vec{E}_1$, $\vec{E}_2$, $\vec{E}_3$ basis of the material frame
$\vec{t}_1$, $\vec{t}_2$, $\vec{t}_3$ basis of the moving frame
$\mathbf{V}$, $\mathbf{V}\left\{\vec{E}_i\right\}$, $\mathbf{V}\left\{\vec{t}_i\right\}$ matrix of a vector/tensor in fixed frame, material frame, and moving frame
X_1, X_2 in-plane coordinates of the points
$\vec{X}$, $\vec{x}$ position vectors in reference configuration and current configuration
A_0, A_t cross-sections in referrence configuration and current configuration
$\vec{\varphi}$, $\overline{\Lambda}$ position vectors and rotation matrix of the centroids
$\vec{\Gamma}$, $\vec{\mathrm{K}}$ translational and rotational strain measures in material description
Γ_1, Γ_2, Γ_3 components of translational strain measures in material frame
ω_1, ω_2, ω_3 components of rotational strain measures in material frame
u_1, u_2 in-plane displacements
ξ_1, ξ_2 deformed cross-section coordinates
γ_1, γ_2 components of derivatives of positions respect to S in current frame
λ, λ_0 stretch in material point and centroids
$\overline{F}$ deformation gradient
ε magnitude of elongation due to bending
W_e, Ψ_e, U_e strain energy density, strain energy, and reduced strain energy
μ_e, $\mu_e^{'}$, E initial shear modulus and Young's modulus
$\overline{C}$, I_1^c Cauchy-Green deformation tensor and its trace
I_1, I_2, J moments of inertia of cross-section
A, A_1, A_2 cross-sectional area and equivalent shear areas
$\vec{N}$, $\vec{M}$ resultant force and moment in material description
$\vec{n}$, $\vec{m}$ resultant force and moment in spatial description
$\vec{n}_{\mathrm{dis}}$, $\vec{m}_{\mathrm{dis}}$ distributed force and torque
$\overline{D}$, $\overline{d}$ tangent elasticity tensor in material and spatial form
$\vec{B}$, $\vec{H}$ magnetic flux density and applied magnetic field
$\vec{B}_r$ residual magnetic flux density in reference configuration
$\vec{B}_a$, $\vec{B}_0$ applied magnetic flux density in the material points and centroids
μ_0 vacuum permeability
W_m, Ψ_m, U_m magnetic free energy density, magnetic free energy, and reduced magnetic free energy
$P(X_1, X_2, S)$ sum of linear terms of X_1 and X_2
$\widetilde{\Phi}$, $\delta\Phi$, Φ_ε arbitrary configuration, variable in specific configuration, and perturbed configuration
$\vec{N}^m$, $\vec{M}^m$, resultant force and moment in material description
$\vec{n}^m_{\mathrm{dis}}$, $\vec{m}^m_{\mathrm{dis}}$ distributed force and torque caused by applied magnetic field
G, g weak form and reduced weak form
$\delta\Phi$, $\Delta\Phi$ combine matrix of variable and increment of configuration
Σ, Ξ operation matrix
$\mathbf{R}$, $\mathbf{R}^m$, $\mathbf{r}_{\mathrm{dis}}$, $\mathbf{r}^m_{\mathrm{dis}}$ combine matrix of force and moment
$L(G)$ linear part of the weak form
Δg_1, Δg_2, Δg_3, increment related part of weak form
L_e^h typical element
N_i shape function
$\mathbf{g}_e^{1h}$, $\mathbf{g}_e^{2h}$, $\mathbf{g}_e^{3h}$ element stiffness matrix
$\mathbf{P}_e^h$ element unbalanced vector
$\overline{P}$, Θ first Piola-Kirchhoff stress tensor and internal power
i, η dumb mark $i = 1, 2, 3$ and $\eta = 1, 2$
$(\cdot)^{'}$, $(\dot{\cdot})$ derivatives of $(\cdot)$ respect to arc length S and time τ
$(\cdot)^{\wedge}$ corresponding skew-symmetric tensor of $(\cdot)$
$\delta(\cdot)$, $\Delta(\cdot)$ variable and increment of $(\cdot)$
$\nabla(\cdot)$ gradient of $(\cdot)$
$(\cdot)_e^h$ approximate variable of $(\cdot)$

and Zhao, 2022). To further develop this advantage of HMS materials, it is essential to investigate the deformation responses of the HMS materials. A mechanics model of the HMS materials is presented by Zhao et al. (Zhao et al., 2019). In their work, the magnetic Cauchy stresses of the ideal HMS materials, which has a residual magnetic flux density and the linear relationship between the induced magnetic flux density and the applied magnetic field, under finite deformation is presented. This simplification is effective but with some limitations, the model cannot predict the deformation of the HMS material under the high applied magnetic field. Based on micropolar continuum theory, Dadgar-Rad and Hossain (Dadgar-Rad and Hossain, 2022) developed a novel model of the HMS materials under finite deformation. In the above two works, the magnetization is assumed to be modulated by the deformation gradient. However, this assumption is proved to be not accurate for large strains by Mukherjee et al. (Mukherjee et al., 2021). Considering the dissipative magnetic response of the HMS materials, Mukherjee et al. (Mukherjee et al., 2021) present a thermodynamically consistent modeling framework for the HMS materials. Their work demonstrates the magnetization of the HMS material only change with rotation, not with stretch. Despite all this, the concise form of the magnetic free energy density presented by Zhao et al. (Zhao et al., 2019) is attractive. We modify the magnetic free energy density by considering an affine rotation of the hard-magnetic particles to address the issue in this work. In addition, Mukherjee et al. (Mukherjee and Danas, 2022) present a novel mechanics model for both hard and soft magnetic materials. Although these models can accurately predict deformations of some HMS structures, the simulations of the HMS structures, especially complex structures, are time-consuming.

To improve the efficiency of the computation models of the HMS structures, researchers have developed a series of HMS rod models with fewer degrees of freedom (DOFs). Some researchers focused on the large bending deformation of the HMS beams with uniform magnetization (Chen and Wang, 2020; Wang et al., 2020; Rajan and Arockiarajan, 2021; Yan et al., 2022), and hyperelastic material models have been utilized to describe the matrix materials in their works. In addition, Chen et al. (Chen et al., 2020; Chen et al., 2020; Chen et al., 2023) developed the mechanics models of the HMS beam with nonuniform magnetization. The viscoelastic effect in the HMS beam was investigated by Dadgar-Rad and Hossain (Dadgar-Rad and Hossain, 2022). Dehrouyeh-Semnani (Dehrouyeh-Semnani, 2021) discussed the buckling problem of the HMS cantilevers. However, the above-mentioned studies focus on the models of the HMS rod under two-dimensional deformation. The two-dimensional assumption may be invalid in certain situations: (1) the external forces other than magnetic forces exert on the beam; (2) the HMS beam with nonuniform magnetization is discussed; (3) the applied magnetic field is nonuniform. Therefore, the three-dimensional models

of HMS rod are desirable. Due to the challenge of dealing with the nonlinearity of three-dimensional finite rotations, the studies on the three-dimensional models of HMS rod are few. Chen et al. (Chen et al., 2021) utilize the three Euler angles to describe the three-dimensional finite rotations, and based on the principle of minimum potential energy, develop the three-dimensional model of HMS rods. Sano et al. (Sano et al., 2022) focus on the three-dimensional Kirchhoff HMS rod in which have regraded the spatially varying magnetic fields. Their models have been proved accurate in some scenes by comparing with the experiments and previous papers. However, their model also assumes that the cross-sections of the rod are rigid and the stress–strain relation of the rod is linear. The drawbacks will make their models inaccurate when the deformation of the rod is large, especially large stretch (Wu et al., 2022). To extend the application of the HMS rod, we develop a mechanics model of the HMS rod under three-dimensional large deformation with deformable cross-section, whose stress–strain relation is described by the incompressible Non-Hookean model.

The rod model including both the large deformation and deformable cross-section can be traced back the work by Simo and Vu-Quoc (Simo and Vu-Quoc, 1991) in which they presented a geometrically-exact rod model including the torsion-warping deformation. They introduced an additional DOF called as “warping amplitude” and the “warping pattern” to describe the out-of-plane warping displacement, and this method has been extended to the special Euclidean group SE(3) by Rong et al. (Rong et al., 2020). In addition, considering the two bending-warping patterns and a torsion-warping pattern, Klinkel and Govindjee (Klinkel and Govindjee, 2003) developed an anisotropic bending-torsion coupling beam model. For the above models, the warping patterns are prescribed, and the common methods to determine the warping patterns are experiments or 3D finite element simulations. Some researchers (Pimenta and Campello, 2003; Dasambiagio et al., 2009; Sokolov et al., 2015) derive the warping patterns from linear elastostatics, which is effective for small strain problems. However, the additional DOFs were still introduced and the coupling between the cross-section deformation modes was not considered. Petrov et al. (Petrov and Géradin, 1998; Petrov and Géradin, 1998) present rods model with deformable cross-section based on St. Venant solution without additional DOFs, however, only the small strain is included in their model. It is difficult to improve existing mechanics model of the rod-like structure actuated by a variety of stimuli including magnetic field based on all above models. Therefore, The soft rod model without additional DOFs is worth to develop. We couple the bending and stretch to obtain a relatively simpler cross-section deformation mode. In addition, the incompressibility of the rod materials is assumed to avoid the additional DOFs. Finally, we establish an explicit and analytical load-deformation relation of the soft rod.

Compared with the previous work, the novel aspects and basic features of this work can be delineated as:

(a) The proposed model of the soft rod with deformation cross-section is full nonlinear, explicit, and analytical. There are no additional DOFs are introduced, which mean other mature rod-like soft structure models can be improved by easily replacing their constitutive equations with ours.
(b) Considering an affine rotation of the hard-magnetic particles, a more accurate magnetic free energy density is presented. In addition, the spatial reduction of the magnetic free energy model with the areal change assumption is formulated.
(c) In experiment aspect, a magnetic field driven rod-torsion experiment is presented in this work, as far as we know, similar experiments have not been presented in literature.

The paper is organized as follows. In Section 2, we derive the equilibrium equations of HMS rod, where the explicit load-deformation relation of the soft rod is obtained. The weak form and finite element formulation of the problem is presented in the Section 3. The performance of the model will be showed by 4 simulation examples and compared with 2 experiments in Section 4. In Section 5, we summarize our results and discuss the limitation and future work.

2. Theoretical formulation

This section presents the nonlinear constitutive equations of the straight soft rod and then describes the elastostatic model of the HMS rod. Finally, based on the finite element method, the computational model of the HMS rod is obtained.

2.1. Kinematics

The present work is based on the four assumptions as follows:

(a) The rod is straight in the reference configuration.
(b) Plane-section assumption holds. A cross-section remains to be a plane after deformation.
(c) The cross-section deformation caused by axial tension or compression, which is isotropic and homogeneous. The cross-section deformation caused by bend, twist, and shear is small and can be ignored.
(d) The change of the axial stretch along the axis can be ignored in calculating deformation gradient.

As illustrated in Fig. 1(a), we pick the point O as the origin and $\left\{\vec{e}_i\right\}$ as the basis of the fixed Cartesian coordinate system. The beam denoted by $\Omega\subset\mathbb{R}^3$ is a non-denumerable set of cross-sections whose centroids are connected by a curve referred to as the line of centroids (Simo, 1985). The cross-sections can be marked by the arc length of the line of centroids in the reference configuration $S\in[0,L]$, and the point in the cross-sections can be marked by the component of the principal axis direction of the distance between the point and the centroid in the reference configuration (X_1,X_2), which is shown in Fig. 1(a). For a straight rod, the position vector $\vec{X}$ of the material point X can be described as

$$\vec{X}(S,X_1,X_2)=\vec{r}_0+S\vec{E}_3+X_\eta\vec{E}_\eta,\quad S\in[0,L], \tag{1}$$

where $\vec{r}_0$ is the position vector of the starting point of the centroid in the reference configuration, $\vec{E}_3$ is the unit vector parallel to the line of centroids in the reference configuration, and the $\vec{E}_\eta$ is the unit vector parallel to centroid principal axis direction.

Remark 2.1. *$\vec{E}_1$, $\vec{E}_2$, and $\vec{E}_3$ form an orthonormal frame referred to as material frame, as illustrated in Fig. 1(a), such that $\vec{E}_3\perp A_0(S)$, where A_0 is the cross-section in the referrence configuration.*

To parameterize the current configuration (deformed configuration) of the rod, an orthonormal frame $\left\{\vec{t}_i(S)\right\}$ is defined and referred to as moving frame, such that

$$\vec{t}_3\perp A_t(S),\quad \frac{\partial\vec{x}(X_1=0,X_2=0)}{\partial X_1}//\vec{t}_1,\quad \vec{t}_2\equiv\vec{t}_3\times\vec{t}_1, \tag{2}$$

where $\vec{x}$ is the position vector of the material point in the current configuration as shown in Fig. 1(a), and A_t is the cross-section in the current configuration. An orthogonal transformation $\bar{\Lambda}$ which defines the relationship between $\left\{\vec{t}_i\right\}$ and $\left\{\vec{E}_i\right\}$ is given by

$$\bar{\Lambda}(S)=\vec{t}_i\otimes\vec{E}_i,\quad \vec{t}_i=\bar{\Lambda}\vec{E}_i. \tag{3}$$

The derivatives of the moving frame can be obtained by

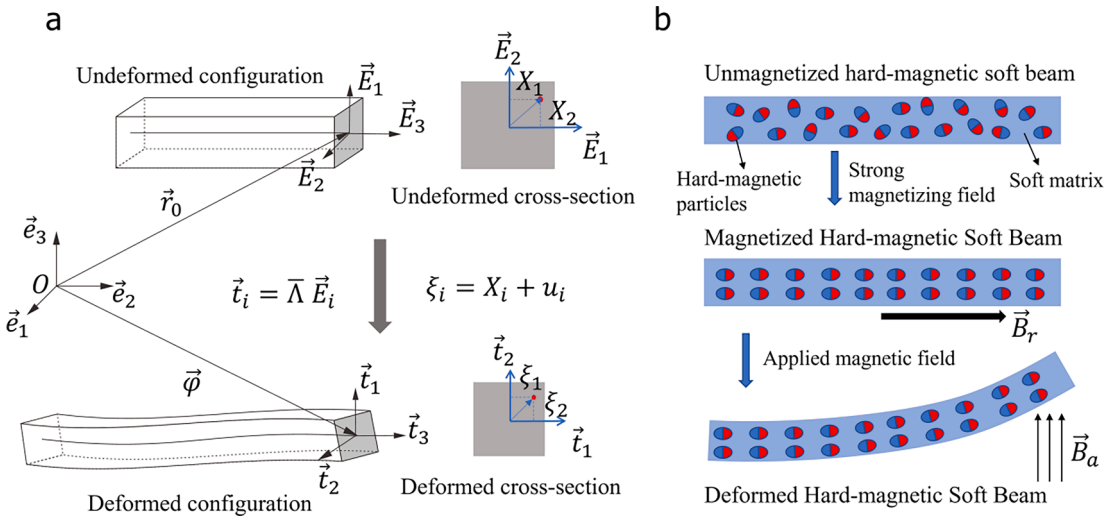

Fig. 1. (a) rod configurations and section shapes before and after deformation. Three orthonormal frames are fixed frame $\left\{\vec{e}_i\right\}$, material frame $\left\{\vec{E}_i\right\}$, and moving frame $\left\{\vec{t}_i\right\}$, respectively. (b) A schematic of the magnetization and deformation process of the hard-magnetic soft rod.

$$\frac{d}{dS}\vec{t}_i = \vec{\omega}\times\vec{t}_i,\quad \vec{\omega} = \omega_1\vec{t}_1+\omega_2\vec{t}_2+\omega_3\vec{t}_3,$$
$$\vec{\omega}^{\wedge} = \left(\frac{d}{dS}\overline{\Lambda}\right)\overline{\Lambda}^{T}, \tag{4}$$

where $(\cdot)^{\wedge}$ represents the corresponding skew-symmetric tensor of the axial vector $(\cdot)$. The material points X are mapped into positions $\vec{x}$ by

$$\begin{aligned}\vec{x}(S,X_1,X_2) &= \vec{\varphi}(S)+[X_\eta+u_\eta(S,X_1,X_2)]\,\vec{t}_\eta\\ &= \vec{\varphi}(S)+\xi_\eta\,\vec{t}_\eta,\end{aligned} \tag{5}$$

where $\vec{\varphi}$ is the position of the centroid in current configuration, u_η is the in-plane displacement, and ξ_η is the deformed cross-section coordinates which is illustrated in Fig. 1(a).

Remark 2.2. *According to Eq. (2) and Eq. (5), u_η should satisfy $u_\eta(S,0,0)=0$ and $\frac{\partial u_2(S,0,0)}{\partial X_1}=0$.*

The partial derivatives of the positions with respect to S can be given by

$$\frac{\partial\vec{x}}{\partial S} = \frac{d}{dS}\vec{\varphi}+\frac{\partial u_\eta}{\partial S}\vec{t}_\eta+\xi_\eta\vec{\omega}\times\vec{t}_\eta = \gamma_\eta\vec{t}_\eta+\lambda\vec{t}_3. \tag{6}$$

In special, the variables in centroids can be obtained by

$$\begin{aligned}\Gamma_\eta &= \gamma_\eta(X_1=0,X_2=0) = \frac{d}{dS}\vec{\varphi}\cdot\vec{t}_\eta,\\ \lambda_0 &= \lambda(X_1=0,X_2=0) = \frac{d}{dS}\vec{\varphi}\cdot\vec{t}_3.\end{aligned} \tag{7}$$

According to the assumption (d), the axial stretch satisfies $\frac{d}{dS}\lambda_0\approx 0$. The deformation gradient denoted by $\overline{F}$ is given by

$$\overline{F} = \frac{\partial\vec{x}}{\partial X_\eta}\otimes\vec{E}_\eta+\frac{\partial\vec{x}}{\partial S}\otimes\vec{E}_3. \tag{8}$$

The soft material in soft robots are generally incompressible, therefore, the $\overline{F}$ should satisfy

$$\begin{aligned}|\overline{F}| &= \left(\frac{\partial\vec{x}}{\partial X_1}\times\frac{\partial\vec{x}}{\partial X_2}\right)\cdot\frac{\partial\vec{x}}{\partial S}\\ &= \left(1+\frac{\partial u_1}{\partial X_1}+\frac{\partial u_2}{\partial X_2}+\frac{\partial u_1}{\partial X_1}\frac{\partial u_2}{\partial X_2}-\frac{\partial u_2}{\partial X_1}\frac{\partial u_1}{\partial X_2}\right)\lambda = 1.\end{aligned} \tag{9}$$

According to the assumption (c), the cross-section deformation is isotropic and homogeneous, such that

$$\frac{\partial u_1}{\partial X_1}=\frac{\partial u_2}{\partial X_2}=\frac{1}{\sqrt{\lambda}}-1\approx\frac{1}{\sqrt{\lambda_0}}-1,\quad \frac{\partial u_1}{\partial X_2}=\frac{\partial u_2}{\partial X_1}=0 \tag{10}$$

Combining with the conditions of REMARK 2.2, u_η and ξ_η can be given by

$$\begin{aligned}u_\eta &\approx \left(\frac{1}{\sqrt{\lambda_0}}-1\right)X_\eta,\\ \xi_\eta &\approx \frac{X_\eta}{\sqrt{\lambda_0}}.\end{aligned} \tag{11}$$

Remark 2.3. *Eq. (11) implies $\lambda\approx\lambda_0$ which mean the normal deformation caused by bend $\xi_\eta\vec{\omega}\times\vec{t}_\eta\sim\varepsilon$ is small. Therefore, the rod model is not very accurate for the thick rod with large bending. For most HMS rod, this rod model is appropriate.*

We ignore the $\frac{d}{dS}\lambda_0$, according to assumption (d), such that

$$\begin{aligned}\lambda &= \lambda_0+\frac{\omega_1X_2-\omega_2X_1}{\sqrt{\lambda_0}},\\ \gamma_1 &= \Gamma_1-\frac{\omega_3X_2}{\sqrt{\lambda_0}},\\ \gamma_2 &= \Gamma_2+\frac{\omega_3X_1}{\sqrt{\lambda_0}}.\end{aligned} \tag{12}$$

Substitute Eq. (6) and Eq. (10) into Eq. (8), the matrix of deformation gradient in the fixed frame $\mathbf{F}$ can be given by

$$\mathbf{F} = \frac{\mathbf{t}_\eta\mathbf{E}_\eta^{\mathrm{T}}}{\sqrt{\lambda}}+\lambda\mathbf{t}_3\mathbf{E}_3^{\mathrm{T}}+\gamma_\eta\mathbf{t}_\eta\mathbf{E}_3^{\mathrm{T}}. \tag{13}$$

In this work, the bold symbols represent the matrix notation of the corresponding vector or tensor. Without specifical mention, the elements of the matrix are the components of the vector or tensor in the fixed Cartesian basis $\left\{\vec{e}_i\right\}$. The $\overline{F}$ in centroids can be obtained by

$$\begin{aligned}\overline{F}_0 &= \overline{F}(X_1=0,X_2=0)\\ &= \overline{\Lambda}\left(\frac{\vec{E}_\eta\otimes\vec{E}_\eta}{\sqrt{\lambda_0}}+\lambda_0\vec{E}_3\otimes\vec{E}_3+\Gamma_\eta\vec{E}_\eta\otimes\vec{E}_3\right).\end{aligned} \tag{14}$$

2.2. Constitutive equations

The incompressible neo-Hookean model which is valid for small and medium strain level (Finney, 2012) is utilized to describe soft material. The strain energy density W_e can be obtained by

$$W_e(S, X_1, X_2) = \frac{\mu_e}{2}\left(I_1^C - 3\right), \tag{15}$$

where μ_e is the initial shear modulus, and I_1^C is the trace of the right Cauchy-Green deformation tensor $\overline{C} = \overline{F}^T\overline{F}$. Using Eq. (13), the matrix of $\overline{C}$ in the material frame $\mathbf{C}_{\left\{\overrightarrow{E}_i\right\}}$ can be given by

$$\mathbf{C}_{\left\{\overrightarrow{E}_i\right\}} = \begin{bmatrix} \frac{1}{\lambda} & 0 & \frac{\gamma_1}{\sqrt{\lambda}} \\ 0 & \frac{1}{\lambda} & \frac{\gamma_2}{\sqrt{\lambda}} \\ \frac{\gamma_1}{\sqrt{\lambda}} & \frac{\gamma_2}{\sqrt{\lambda}} & \lambda^2 + \gamma_1^2 + \gamma_2^2 \end{bmatrix}. \tag{16}$$

Thus I_1^C can be given by

$$\begin{aligned} I_1^C &= \lambda^2 + \frac{2}{\lambda} + \gamma_1^2 + \gamma_2^2 \\ &= \lambda_0^2 + \frac{2}{\lambda_0} + \Gamma_1^2 + \Gamma_2^2 \\ &+ \left(2\lambda_0 - \frac{2}{\lambda_0^2}\right)\frac{(\omega_1 X_2 - \omega_2 X_1)}{\sqrt{\lambda_0}} + \left(\frac{1}{\lambda_0} + \frac{2}{\lambda_0^4}\right)(\omega_1 X_2 - \omega_2 X_1)^2 \\ &+ \frac{2\omega_3(X_1\Gamma_2 - X_2\Gamma_1)}{\sqrt{\lambda_0}} + \frac{\omega_3^2\left(X_1^2 + X_2^2\right)}{\lambda_0} + o\left(\varepsilon^2\right) \end{aligned} \tag{17}$$

By ignoring the small quantity, a reduced expression of the strain energy per unit of arc length in the reference configuration U_e can be given by

$$\begin{aligned} U_e(S) &= \iint_{A_0} W_e dX_1 dX_2 = \iint_{A_0} \frac{\mu_e}{2}\left(I_1^C - 3\right) dX_1 dX_2 \\ &= \mu_e A\left(\frac{\lambda_0^2}{2} + \frac{1}{\lambda_0} - 3\right) + \frac{\mu_e A_1}{2}\Gamma_1^2 + \frac{\mu_e A_2}{2}\Gamma_2^2 + \left(\frac{1}{2\lambda_0} + \frac{1}{\lambda_0^4}\right)\left(\mu_e I_1\omega_1^2 + \mu_e I_2\omega_2^2\right) + \frac{\mu_e J\omega_3^2}{2\lambda_0}, \end{aligned} \tag{18}$$

where A is the area of the cross-section in the reference configuration, $I_1 = \iint_A X_2^2 dX_1 dX_2$ and $I_2 = \iint_A X_1^2 dX_1 dX_2$ are the moments of inertia of the cross-section, and $J = I_1 + I_2$ is the polar moment of inertia of the cross-section. $A_\eta = k_\eta A$ is the equivalent shear area where k_η is the reasonable factor (Bathe, 2014). It should be noted that the reason we ignore the small quantity to avoid the numerical integration is to obtain explicit and analytical forms of the constitutive equations which can improve the computation efficiency. Following the previous works (Simo, 1985; Crisfield and Jelenić, 1999; Li et al., 2022), we define the translational and rotational strain measures in the material description $\overrightarrow{\Gamma}(S)$ and $\overrightarrow{\mathrm{K}}(S)$ as

$$\begin{aligned} \overrightarrow{\Gamma} &= \overline{\Lambda}^T\left(\frac{d}{dS}\overrightarrow{\varphi} - \overrightarrow{t}_3\right) = \Gamma_i\overrightarrow{E}_i, \\ \overrightarrow{\mathrm{K}} &= \overline{\Lambda}^T\overrightarrow{\omega} = \omega_i\overrightarrow{E}_i, \end{aligned} \tag{19}$$

where $\Gamma_3 = \lambda_0 - 1$. The strain measures is conjugate to the resultant force and moment (see Appendix A) over the cross-section per unit of reference arc length in the material description $\overrightarrow{N}(S)$ and $\overrightarrow{M}(S)$, which is defined as

$$\begin{aligned} \overrightarrow{N} &= \Lambda^T\overrightarrow{n} = \frac{\partial U_e}{\partial\overrightarrow{\Gamma}}, \\ \overrightarrow{M} &= \Lambda^T\overrightarrow{m} = \frac{\partial U_e}{\partial\overrightarrow{\mathrm{K}}}, \end{aligned} \tag{20}$$

where $\overrightarrow{n}$ and $\overrightarrow{m}$ are the resultant force and moment in the spatial description. And the equilibrium equations of the (non-magnetic) rod which were first proposed by Simo (Simo, 1985) and may be given by

$$\begin{aligned} \frac{d}{dS}\overrightarrow{n} + \overrightarrow{n}_{\mathrm{dis}} &= 0, \\ \frac{d}{dS}\overrightarrow{m} + \frac{d}{dS}\overrightarrow{\varphi} \times \overrightarrow{n} + \overrightarrow{m}_{\mathrm{dis}} &= 0, \end{aligned} \tag{21}$$

where $\overrightarrow{n}_{\mathrm{dis}}$ and $\overrightarrow{m}_{\mathrm{dis}}$ are the distributed force and torque per unit of reference arc length. Substituting Eq (18) to Eq (20), we can get

$$\mathbf{N}_{\left\{\overrightarrow{E}_i\right\}} = \begin{bmatrix} \mu_e A_1\Gamma_1 \\ \mu_e A_2\Gamma_2 \\ \mu_e A\left(\lambda_0 - \frac{1}{\lambda_0^2}\right) - \left(\frac{1}{2\lambda_0^2} + \frac{4}{\lambda_0^5}\right)\left(\mu_e I_1\omega_1^2 + \mu_e I_2\omega_2^2\right) - \frac{\mu_e J\omega_3^2}{2\lambda_0^2} \end{bmatrix}, \quad \mathbf{M}_{\left\{\overrightarrow{E}_i\right\}} = \begin{bmatrix} \left(\frac{1}{\lambda_0} + \frac{2}{\lambda_0^4}\right)\mu_e I_1\omega_1 \\ \left(\frac{1}{\lambda_0} + \frac{2}{\lambda_0^4}\right)\mu_e I_2\omega_2 \\ \frac{\mu_e J\omega_3}{\lambda_0} \end{bmatrix}. \tag{22}$$

The matrix of tangent elasticity tensor $\mathbf{D}$ is defined as

$$\mathbf{D} = \begin{bmatrix} \frac{\partial \mathbf{N}}{\partial \mathbf{\Gamma}} & \frac{\partial \mathbf{N}}{\partial \mathbf{K}} \\ \frac{\partial \mathbf{M}}{\partial \mathbf{\Gamma}} & \frac{\partial \mathbf{M}}{\partial \mathbf{K}} \end{bmatrix} = \begin{bmatrix} \frac{\partial^2 U_e}{\partial \mathbf{\Gamma} \partial \mathbf{\Gamma}} & \frac{\partial^2 U_e}{\partial \mathbf{\Gamma} \partial \mathbf{K}} \\ \frac{\partial^2 U_e}{\partial \mathbf{K} \partial \mathbf{\Gamma}} & \frac{\partial^2 U_e}{\partial \mathbf{K} \partial \mathbf{K}} \end{bmatrix}. \tag{23}$$

And the tangent elasticity matrix in the material frame $\mathbf{D}_{\left\{\vec{E}_i\right\}}$ can be given by

$$\mathbf{D}_{\left\{\vec{E}_i\right\}} = \mu_e \begin{bmatrix} A_1 & & & & & \\ 0 & A_2 & & & & \\ 0 & 0 & A\left(1+\frac{2}{\lambda_0^3}\right)+\left(\frac{1}{\lambda_0^3}+\frac{20}{\lambda_0^6}\right)\left(\mu I_1 \omega_1^2+\mu I_2 \omega_2^2\right)+\frac{\mu J \omega_3^2}{\lambda_0^3} & & & \\ 0 & 0 & -\omega_1 I_1\left(\frac{1}{\lambda_0^2}+\frac{8}{\lambda_0^5}\right) & I_1\left(\frac{1}{\lambda_0}+\frac{2}{\lambda_0^4}\right) & & \\ 0 & 0 & -\omega_2 I_2\left(\frac{1}{\lambda_0^2}+\frac{8}{\lambda_0^5}\right) & 0 & I_2\left(\frac{1}{\lambda_0}+\frac{2}{\lambda_0^4}\right) & \\ 0 & 0 & -\frac{\mu J \omega_3}{\lambda_0^2} & 0 & 0 & \frac{J}{\lambda_0} \end{bmatrix}. \tag{24}$$

Remark 2.4. *When the deformation of the beam is small, the beam model degenerates into the linear elastic constitutive model and the "tangent elasticity matrix" degenerates into*.

$$\lim_{\mathbf{\Gamma}, \mathbf{K} \to 0} \mathbf{D}_{\left\{\vec{E}_i\right\}} = \begin{bmatrix} \mu_e A_1 & 0 & 0 & 0 & 0 & 0 \\ 0 & \mu_e A_2 & 0 & 0 & 0 & 0 \\ 0 & 0 & EA & 0 & 0 & 0 \\ 0 & 0 & 0 & EI_1 & 0 & 0 \\ 0 & 0 & 0 & 0 & EI_2 & 0 \\ 0 & 0 & 0 & 0 & 0 & \mu_e J \end{bmatrix} \tag{25}$$

where $E = 3\mu_e$ is the Young's modulus.

2.3. Derivation of the equilibrium equations of the HMS rod

Now we focus on a soft rod with hard-magnetic properties (HMS rod), which achieves lagre deformation under the applied magnetic field as shown in Fig. 1(b). In this work, we assume the HMS material is an ideal HMS material whose magnetic flux density $\vec{B}$ is linearly related to the applied magnetic field $\vec{H}$ and their relation can be given by

$$\vec{H} = \frac{1}{\mu_0}\left[\vec{B} - \vec{B}_r(S)\right], \tag{26}$$

where $\vec{B}_r$ is the residual magnetic flux density in the reference configuration, and μ_0 is the vacuum permeability. The Eq. (26) indicates that the residual magnetic flux density $\vec{B}_r$ is only the function of the arc length of the line of centroids S, which means the residual magnetic flux density at all points of the same cross-section is identical. Note that the residual magnetic flux density in the reference configuration $\vec{B}_r$ does not change with the deformation. In addition, The magnetic free energy density of the ideal HMS material can be given by (Zhao et al., 2019)

$$W_m(X_1, X_2, S) = -\frac{1}{\mu_0}\vec{B}_a(\vec{x})\cdot\overline{F}\vec{B}_r, \tag{27}$$

where $\vec{B}_a = \mu_0 \vec{H}$ is the applied magnetic flux density. It should be noted that assuming $\vec{B}_a$ is known and unaltered is a simplification. The magnetic dipole moments of the hard-magnetic particles will affect the distribution of the applied magnetic flux density. According to the work presented by Mukherjee et al. (Mukherjee et al., 2021), the magnetic free energy density $\vec{B}_r$ should not change with the stretch when the matrix is far softer than the particles, because the particles can only rotate without deformation. To address this issue, we assume that the particles rotate affinely with the macroscopic rotation $\overline{\Lambda}$, in which the shear effect is ignored, and the magnetic free energy density of the ideal HMS material can be modified as

$$\begin{aligned} W_m(X_1, X_2, S) &= -\frac{1}{\mu_0}\vec{B}_a(\vec{x})\cdot\overline{\Lambda}\vec{B}_r \\ &= -\frac{1}{\mu_0}\vec{B}_0(S)\cdot\overline{\Lambda}\vec{B}_r + Z(X_1, X_2, S), \end{aligned} \tag{28}$$

In particular, the applied magnetic flux density in the centroid is $\vec{B}_0 = \vec{B}_a(\vec{\varphi})$, $Z(X_1, X_2, S)$ is the sum of linear terms of X_1 and X_2. In this work, only the gradient invariant applied magnetic field is considered. Then, the reduced expression of magnetic free energy per unit of reference arc length U_m can be given by

$$U_m = \iint_{A_0} W_m dX_1 dX_2 = -\frac{A}{\mu_0}\vec{B}_0\cdot\overline{\Lambda}\vec{B}_r. \tag{29}$$

Consider an arbitrary configuration of the rod $\widetilde{\Phi} = \left\{\widetilde{\varphi}, \widetilde{\Lambda}\right\}$, which is specified by the position of its line of the centroids and the moving frame. In this work, a variable with a tilde above it represents the variable in the specific configuration $\widetilde{\Phi}$. In addition, we consider any infinitesimal admissible variation $\delta\Phi = \left\{\delta\vec{\varphi}, \delta\vec{\theta}\right\}$, and the perturbed configuration $\Phi_\varepsilon = \left\{\vec{\varphi}_\varepsilon, \overline{\Lambda}_\varepsilon\right\}$ can be given by

$$\begin{aligned} \vec{\varphi}_\varepsilon &= \widetilde{\varphi} + \delta\vec{\varphi}, \\ \overline{\Lambda}_\varepsilon &= \exp\left(\delta\vec{\theta}\right)\widetilde{\Lambda}. \end{aligned} \tag{30}$$

Based on Eq. (30), the variation of $\overline{\Lambda}$ can be given by

$$\delta\overline{\Lambda} = \exp\left(\delta\overrightarrow{\theta}^{\wedge}\right)\widetilde{\Lambda} - \widetilde{\Lambda} = \delta\overrightarrow{\theta}^{\wedge}\widetilde{\Lambda}. \tag{31}$$

The variation of the strain measures $\overrightarrow{\Gamma}$ and $\overrightarrow{K}$ can be given by

$$\begin{aligned} \delta\overrightarrow{\Gamma} &= \widetilde{\Lambda}^{T}\left[\delta\overrightarrow{\varphi}' + (\widetilde{\varphi}')^{\wedge}\delta\overrightarrow{\theta}\right], \\ \delta\overrightarrow{K} &= \widetilde{\Lambda}^{T}\delta\overrightarrow{\theta}'. \end{aligned} \tag{32}$$

The variation of U_m can be given by

$$\delta U_m = -\widetilde{n}^{m}_{\mathrm{dis}}\cdot\delta\overrightarrow{\varphi} - \widetilde{m}^{m}_{\mathrm{dis}}\cdot\delta\overrightarrow{\theta} + \widetilde{N}^{m}\cdot\delta\overrightarrow{\Gamma} + \widetilde{M}^{m}\cdot\delta\overrightarrow{K}, \tag{33}$$

where $\overrightarrow{n}^{m}_{\mathrm{dis}}$ and $\overrightarrow{m}^{m}_{\mathrm{dis}}$ are the distributed force and torque per unit of reference arc length caused by applied magnetic field, and $\overrightarrow{N}^{m}$ and $\overrightarrow{M}^{m}$ are the resultant force and moment in the material description caused by applied magnetic field. Substituting Eq. (29) into Eq.(33), we can get

$$\begin{aligned} \overrightarrow{n}^{m}_{\mathrm{dis}} &= \frac{A}{\mu_0}\left(\nabla\overrightarrow{\mathrm{B}}_0\right)^{T}\overline{\Lambda}\overrightarrow{B}_r, \\ \overrightarrow{m}^{m}_{\mathrm{dis}} &= \frac{A}{\mu_0}\left(\overline{\Lambda}\overrightarrow{B}_r\right)\times\overrightarrow{B}_0, \end{aligned} \tag{34}$$

where $\nabla\overrightarrow{\mathrm{B}}_0$ is the gradient of $\overrightarrow{B}_0$, and

$$\mathbf{N}^{m}\left\{\overrightarrow{E}_i\right\} = \mathbf{M}^{m}\left\{\overrightarrow{E}_i\right\} = \begin{bmatrix} 0 \\ 0 \\ 0 \end{bmatrix}. \tag{35}$$

Hence, the equilibrium equations of the HMS rod can be given by

$$\begin{aligned} \frac{d}{dS}\overrightarrow{n} + \overrightarrow{n}_{\mathrm{dis}} + \overrightarrow{n}^{m}_{\mathrm{dis}} &= 0, \\ \frac{d}{dS}\overrightarrow{m} + \frac{d}{dS}\overrightarrow{\varphi}\times\overrightarrow{n} + \overrightarrow{m}_{\mathrm{dis}} + \overrightarrow{m}^{m}_{\mathrm{dis}} &= 0, \end{aligned} \tag{36}$$

3. Finite element formulation

In this section, we present the weak form of the problem discussed in Section 2, and its linearization is deduced. Next, we consider the finite element formulation of the lineraization of the weak form. In addition, the matrix equations of the problem is presented.

3.1. Weak form of the equilibrium equations of the HMS beam

The weak form of the equilibrium equations of the HMS rod in matrix form can be given by

$$\begin{aligned} G(\widetilde{\Phi}, \delta\Phi) = &\int_L\left[\frac{d}{dS}\mathbf{n}^{T}\delta\boldsymbol{\varphi} + \left(\frac{d}{dS}\mathbf{m} + \frac{d}{dS}\boldsymbol{\varphi}^{\wedge}\mathbf{n}\right)^{T}\delta\boldsymbol{\theta}\right]dS \\ &+\int_L\left[\left(\mathbf{n}_{\mathrm{dis}} + \mathbf{n}^{m}_{\mathrm{dis}}\right)^{T}\delta\boldsymbol{\varphi} + \left(\mathbf{m}_{\mathrm{dis}} + \mathbf{m}^{m}_{\mathrm{dis}}\right)^{T}\delta\boldsymbol{\theta}\right]dS = 0. \end{aligned} \tag{37}$$

Integration by parts of Eq. (37) lead to

$$\begin{aligned} G = &\int_L\left[\mathbf{n}^{T}(\delta\boldsymbol{\varphi}' - \delta\boldsymbol{\theta}^{\wedge}\boldsymbol{\varphi}') + \mathbf{m}^{T}\delta\boldsymbol{\theta}'\right]dS \\ &-\int_L\left[\left(\mathbf{n}_{\mathrm{dis}} + \mathbf{n}^{m}_{\mathrm{dis}}\right)^{T}\delta\boldsymbol{\varphi} + \left(\mathbf{m}_{\mathrm{dis}} + \mathbf{m}^{m}_{\mathrm{dis}}\right)^{T}\delta\boldsymbol{\theta}\right]dS + b, \end{aligned} \tag{38}$$

where b is the value related to prescribed boundary conditions. In addition, the weak form in the material description can be expressed as

$$\begin{aligned} G = &\int_L\left[\mathbf{N}^{T}\boldsymbol{\Lambda}^{T}(\delta\boldsymbol{\varphi}' - \delta\boldsymbol{\theta}^{\wedge}\varphi') + \mathbf{M}^{T}\boldsymbol{\Lambda}^{T}\delta\boldsymbol{\theta}'\right]dS \\ &-\int_L\left[\left(\mathbf{n}_{\mathrm{dis}} + \mathbf{n}^{m}_{\mathrm{dis}}\right)^{T}\delta\boldsymbol{\varphi} + \left(\mathbf{m}_{\mathrm{dis}} + \mathbf{m}^{m}_{\mathrm{dis}}\right)^{T}\delta\boldsymbol{\theta}\right]dS + b. \end{aligned} \tag{39}$$

The weak form can be expressed as a more compact form by the following notation

$$\begin{aligned} \delta\boldsymbol{\Phi} &= \begin{bmatrix}\delta\boldsymbol{\varphi} \\ \delta\boldsymbol{\theta}\end{bmatrix}, \quad \boldsymbol{\Sigma} = \begin{bmatrix}\boldsymbol{\Lambda} & \mathbf{0} \\ \mathbf{0} & \boldsymbol{\Lambda}\end{bmatrix}, \quad \boldsymbol{\Xi}^{T} = \begin{bmatrix}\frac{d}{dS}\mathbf{1} & \boldsymbol{\varphi}'^{\wedge} \\ 0 & \frac{d}{dS}\mathbf{1}\end{bmatrix}, \\ \mathbf{R} &= \begin{bmatrix}\mathbf{N} \\ \mathbf{M}\end{bmatrix}, \quad \mathbf{r}_{\mathrm{dis}} = \begin{bmatrix}\mathbf{n}_{\mathrm{dis}} \\ \mathbf{m}_{\mathrm{dis}}\end{bmatrix}, \quad \mathbf{r}^{m}_{\mathrm{dis}} = \begin{bmatrix}\mathbf{n}^{m}_{\mathrm{dis}} \\ \mathbf{m}^{m}_{\mathrm{dis}}\end{bmatrix}. \end{aligned} \tag{40}$$

With the notation, the weak form can be recast as

$$\begin{aligned} G &= \int_L\left[\left(\boldsymbol{\Xi}^{T}\delta\boldsymbol{\Phi}\right)^{T}\boldsymbol{\Sigma}\mathbf{R} - \delta\boldsymbol{\Phi}^{T}\left(\mathbf{r}_{\mathrm{dis}} + \mathbf{r}^{m}_{\mathrm{dis}}\right)\right]dS + b \\ &= \int_L g(S)dS + b \end{aligned} \tag{41}$$

where g is the contribution per unit of the reference arc length to the weak form.

3.2. The linearization of the weak form

In our model, the gradient of $\overrightarrow{B}_0$ is a constant. In order to obtain the tangent stiffness matrix, we introduce the linear part of the weak form $L(G)$ defined by

$$L(G) = G(\widetilde{\Phi}, \delta\boldsymbol{\Phi}, 0) + \int_L\left[\frac{\partial g(\widetilde{\Phi}, \delta\boldsymbol{\Phi}, \Delta\boldsymbol{\Phi})}{\partial\Delta\boldsymbol{\Phi}}\bigg|_{\Delta\boldsymbol{\Phi}=0}\Delta\boldsymbol{\Phi}\right]dS, \tag{42}$$

where $\Delta\Phi$ is the incremental displacement and rotation field defined as

$$\Delta\boldsymbol{\Phi} = \begin{bmatrix}\Delta\boldsymbol{\varphi} \\ \Delta\boldsymbol{\theta}\end{bmatrix}. \tag{43}$$

The weak form in the second term of Eq. (42) can be given by

$$g(\widetilde{\Phi}, \delta\boldsymbol{\Phi}, \Delta\boldsymbol{\Phi}) = g(\Phi, \delta\boldsymbol{\Phi}), \tag{44}$$

and the update scheme of Φ can be given by

$$\begin{aligned} \overrightarrow{\varphi} &= \widetilde{\varphi} + \Delta\overrightarrow{\varphi}, \\ \overline{\Lambda} &= \exp\left(\Delta\overrightarrow{\theta}\right)\widetilde{\Lambda}. \end{aligned} \tag{45}$$

The second term in the Eq. (42) can be divided into four parts: the contribution associated with

The elastic resultant force and moment Δg_1, the geometric Δg_2, and the magnetic distributed force and moment Δg_3

$$\begin{aligned} \Delta g_1 &= \int_L\left[(\widetilde{\boldsymbol{\Xi}}^{T}\delta\boldsymbol{\Phi})^{T}\widetilde{\boldsymbol{\Sigma}}\left(\frac{\partial\mathbf{R}}{\partial\Delta\boldsymbol{\Phi}}\bigg|_{\Delta\boldsymbol{\Phi}=0}\right)\Delta\boldsymbol{\Phi}\right]dS, \\ \Delta g_2 &= \int_L\left[\widetilde{\mathbf{R}}^{T}\frac{\partial\left(\boldsymbol{\Sigma}^{T}\boldsymbol{\Xi}^{T}\delta\boldsymbol{\Phi}\right)}{\partial\Delta\boldsymbol{\Phi}}\bigg|_{\Delta\boldsymbol{\Phi}=0}\Delta\boldsymbol{\Phi}\right]dS, \\ \Delta g_3 &= -\int_L\left[\delta\boldsymbol{\Phi}^{T}\left(\frac{\partial\mathbf{r}^{m}_{\mathrm{dis}}}{\partial\Delta\boldsymbol{\Phi}}\bigg|_{\Delta\boldsymbol{\Phi}=0}\right)\Delta\boldsymbol{\Phi}\right]dS. \end{aligned} \tag{46}$$

The linearized elastic force can be expressed by

$$\begin{aligned} \frac{\partial\mathbf{R}}{\partial\Delta\boldsymbol{\Phi}}\bigg|_{\Delta\boldsymbol{\Phi}=0}\Delta\Phi &= \widetilde{\mathbf{D}}\left.\begin{bmatrix}\frac{\partial\boldsymbol{\Gamma}}{\partial\Delta\boldsymbol{\varphi}} & \frac{\partial\boldsymbol{\Gamma}}{\partial\Delta\boldsymbol{\theta}} \\ \frac{\partial\mathbf{K}}{\partial\Delta\boldsymbol{\varphi}} & \frac{\partial\mathbf{K}}{\partial\Delta\boldsymbol{\theta}}\end{bmatrix}\right|_{\Delta\boldsymbol{\Phi}=0}\Delta\boldsymbol{\Phi} \\ &= \widetilde{\mathbf{D}}\widetilde{\boldsymbol{\Sigma}}^{T}\widetilde{\boldsymbol{\Xi}}^{T}\Delta\boldsymbol{\Phi}. \end{aligned} \tag{47}$$

In addition, the first part can be given by

$$\Delta g_1 = \int_L\left[(\widetilde{\boldsymbol{\Xi}}^{T}\delta\boldsymbol{\Phi})^{T}\mathbf{d}\widetilde{\boldsymbol{\Xi}}^{T}\Delta\boldsymbol{\Phi}\right]dS, \tag{48}$$

where $\tilde{\mathbf{d}} = \tilde{\boldsymbol{\Sigma}}\tilde{\mathbf{D}}\tilde{\boldsymbol{\Sigma}}^T$ is the spatial form of the tangent elasticity tensor.

The geometric part contribution Δg_2 can be given by

$$\Delta g_2 = \int_L \left[\left(\mathbf{Y}^T \delta\boldsymbol{\Phi}\right)^T \tilde{\mathbf{Q}} \mathbf{Y}^T \Delta\boldsymbol{\Phi} \right] dS, \tag{49}$$

where the $\mathbf{Y}$ and $\mathbf{Q}$ are defined by

$$\mathbf{Y} = \begin{bmatrix} \frac{d}{dS}\mathbf{1} & \mathbf{0} & \mathbf{0} \\ \mathbf{0} & \frac{d}{dS}\mathbf{1} & \mathbf{1} \end{bmatrix}, \quad \mathbf{Q} = \begin{bmatrix} \mathbf{0} & \mathbf{0} & -\mathbf{n}^\wedge \\ \mathbf{0} & \mathbf{0} & -\mathbf{m} \\ \mathbf{n}^\wedge & \mathbf{0} & \mathbf{n}\boldsymbol{\varphi}'^T - \mathbf{n}^T\boldsymbol{\varphi}'\mathbf{1} \end{bmatrix}. \tag{50}$$

Finally, the last part Δg_3 can be given by

$$\Delta g_3 = -\int_L \left(\delta\boldsymbol{\Phi}^T \tilde{\mathbf{q}} \Delta\boldsymbol{\Phi}\right) dS, \tag{51}$$

where $\mathbf{q}$ is defined by

$$\mathbf{q} = \frac{A}{\mu_0} \begin{bmatrix} 0 & -(\nabla\mathbf{B}_0)^T(\boldsymbol{\Lambda}\mathbf{B}_r)^\wedge \\ (\boldsymbol{\Lambda}\mathbf{B}_r)^\wedge \nabla\mathbf{B}_0 & \mathbf{B}_0^\wedge(\boldsymbol{\Lambda}\mathbf{B}_r)^\wedge \end{bmatrix}. \tag{52}$$

3.3. Finite element approximation

A standard finite element mesh $[0, L] = \cup_{e=1}^{n_e} L_e^h$ is considered, where L_e^h is a typical element with a length h, and n_e is the number of elements. The approximate incremental displacement and rotation field $\Delta\Phi^h$ are given by

$$\Delta\boldsymbol{\varphi}^h(S) = \sum_{i=1}^{n_n} N_i(S)\Delta\boldsymbol{\varphi}_i^h, \quad \Delta\boldsymbol{\theta}^h(S) = \sum_{i=1}^{n_n} N_i(S)\Delta\boldsymbol{\theta}_i^h, \tag{53}$$

where n_n is the number of the nodes, N_i is the shape function associated with the node i, and $\Delta\boldsymbol{\varphi}_i^h$, $\Delta\boldsymbol{\theta}_i^h$ are the approximated incremental displacement and rotation field at the node i.

Substiting the Eq. (53) into the Eq. (42), the weak form of the problem related to the element I_e^h can be given by

$$L\left[G_e^h\right] = \delta\boldsymbol{\Phi}^{hT}\left[\left(\mathbf{g}_e^{1h} + \mathbf{g}_e^{2h} + \mathbf{g}_e^{3h}\right)\Delta\boldsymbol{\Phi}_e^h + \mathbf{P}_e^h\right], \tag{54}$$

where $\mathbf{g}_e^{ih}$ is the element stiffness matrix associated with Δg_i, and $\mathbf{P}_e^h$ is the element unbalanced vector. We denote the submatrices coupling node I and J in $\mathbf{g}_e^{ih}$ by $\mathbf{g}_{eIJ}^{ih}$. From Eq. (48), the $\mathbf{g}_{eIJ}^{1h}$ can be expressed by

$$\mathbf{g}_{eIJ}^{1h} = \int_{L_e^h} \left(\tilde{\boldsymbol{\Xi}}_I^h \mathbf{d}_e \tilde{\boldsymbol{\Xi}}_J^{hT}\right) dS, \tag{55}$$

where $\tilde{\mathbf{d}}_e^h = \tilde{\boldsymbol{\Sigma}}^h \tilde{\mathbf{D}}_e^h \tilde{\boldsymbol{\Sigma}}^{hT}$, and the $\tilde{\boldsymbol{\Xi}}_I^h$ is defined as

$$\tilde{\boldsymbol{\Xi}}_I^h = \begin{bmatrix} N_I'\mathbf{1} & \mathbf{0} \\ -N_I\tilde{\boldsymbol{\varphi}}^\wedge & N_I'\mathbf{1} \end{bmatrix}. \tag{56}$$

The third part $\mathbf{g}_{eIJ}^{2h}$ associated with the geometric contribution can be given by

$$\mathbf{g}_{eIJ}^{2h} = \int_{L_e^h} \begin{bmatrix} \mathbf{0} & -N_I'N_J(\tilde{\mathbf{n}}^h)^\wedge \\ N_IN_J'(\tilde{\mathbf{n}}^h)^\wedge & -N_I'N_J(\tilde{\mathbf{m}}^h)^\wedge + N_IN_J\left\{(\tilde{\mathbf{n}}^h)\boldsymbol{\varphi}'^\sim + (\tilde{\mathbf{n}}^h)^T\boldsymbol{\varphi}'^\sim\mathbf{1}\right\} \end{bmatrix} dS. \tag{57}$$

The last term $\mathbf{g}_{eIJ}^{3h}$, which is associated with the distributed magnetic force and moment, can be given by

$$\mathbf{g}_{eIJ}^{3h} = \int_{L_e^h} \frac{A}{\mu_0} \begin{bmatrix} 0 & N_IN_J(\nabla\mathbf{B}_0)^T\left(\tilde{\boldsymbol{\Lambda}}\mathbf{B}_r\right)^\wedge \\ -N_IN_J\left(\tilde{\boldsymbol{\Lambda}}\mathbf{B}_r\right)^\wedge\nabla\mathbf{B}_0 & -N_IN_J\mathbf{B}_0^\wedge\left(\tilde{\boldsymbol{\Lambda}}\mathbf{B}_r\right)^\wedge \end{bmatrix} dS \tag{58}$$

Finally, $\mathbf{P}_{eI}^h$, the element unbalanced vector at the node I, is given by

$$\mathbf{P}_{eI}^h = \int_{L_e^h} \left\{ \tilde{\boldsymbol{\Xi}}_I^h \left(\tilde{\mathbf{R}}^h + \tilde{\mathbf{R}}^{hm}\right) - \begin{bmatrix} N_I\mathbf{1} & \mathbf{0} \\ \mathbf{0} & N_I\mathbf{1} \end{bmatrix} \left(\tilde{\mathbf{r}}_{\text{dis}}^h + \tilde{\mathbf{r}}_{dis}^{hm}\right) \right\} dS. \tag{59}$$

4. Experiments, numerical simulation, and validation

In this section, some numerical examples and experiments are presented to verify the accuracy of the model. The elements used in this section are quadratic three-node elements, and the reduced integration is utilized to avoid the shear locking (Simo and Vu-Quoc, 1986). The iterative solution procedure follows Li et al. (Li et al., 2022).

4.1. Experiment methods

The hard-magnetic soft materials of rods are prepared by mixing the NdFeB powder with the silicon rubber E605 (Hong Ye Silicone). The mixture (Mass density $\rho = 1869.7 \pm 32.4\text{kg/m}^3$) is poured into the mold prepared in advance and then cured for 4 h at 45℃. After demoulding, the material is magnetized by applying a strong magnetic field. The strong magnetic field is producted by a high magnetic field generator (Shen Zhen He Sheng Hui Electronics Co. Ltd) as shown in Fig. 2(a).

We obtain the initial shear modulus of the material by fitting stress–strain data with the incompressible neo-Hookean model. The stress–strain data is presented by the uniaxial tensile experiments which are conducted on ESM303 force test stands (Mark-10) depicted as Fig. 2 (b). As some researchers mentioned (Garcia-Gonzalez et al., 2023), the dipole–dipole interactions of the particles will enhance the stretch

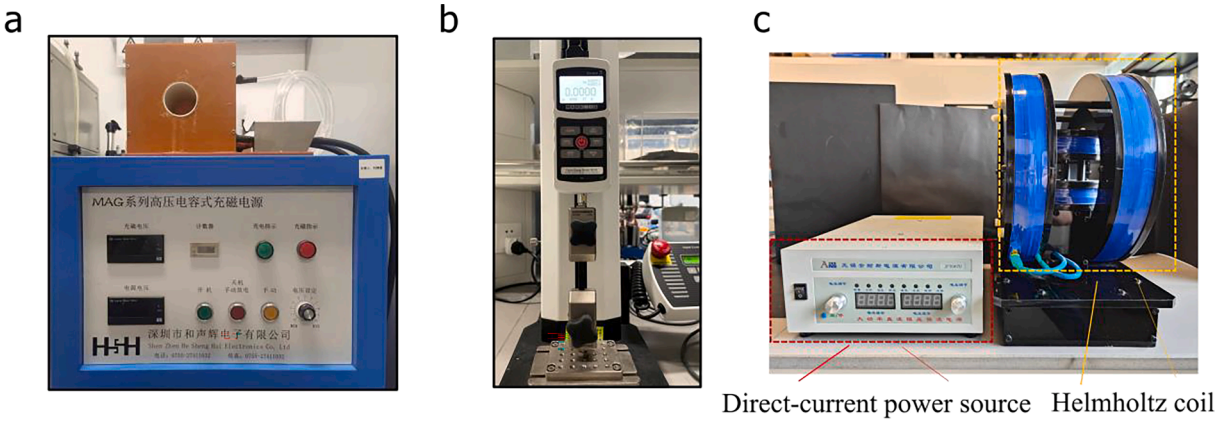

Fig. 2. (a) High magnetic field generator. (b) ESM303 force test stands. (c) applied magnetic field generating device.

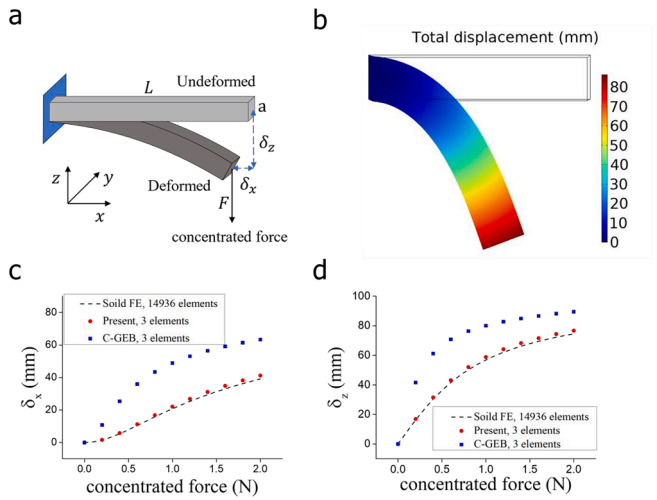

Fig. 3. (a) Schematic of the rod subjected to a concentrated force F. The rod length, side length of cross-section, and the magnitude of the tip displacement are prescribed as $L = 100\,\text{mm}$, $a = 20\,\text{mm}$, δ_x and δ_z. (b) Total displacement of the rod subjected to a concentrated force $F = 2\,\text{N}$. (c) magnitudes of the tip displacement in x-direction δ_x with the different concentrated force of the simulation results. Black line are the results obtained with three-dimensional soild finite element model (14936 tetraheron elements), pink dots are the results obtained with present HMS rod model with 3 elements (quadratic elements), and blue dots are the results obtained with classic geometrically exact beam (C-GEB) model with 3 element (quadratic elements). (d) magnitudes of the tip displacement in z-direction δ_z with the different concentrated force of the simulation results. The meaning of the legend is the same as that in (c).

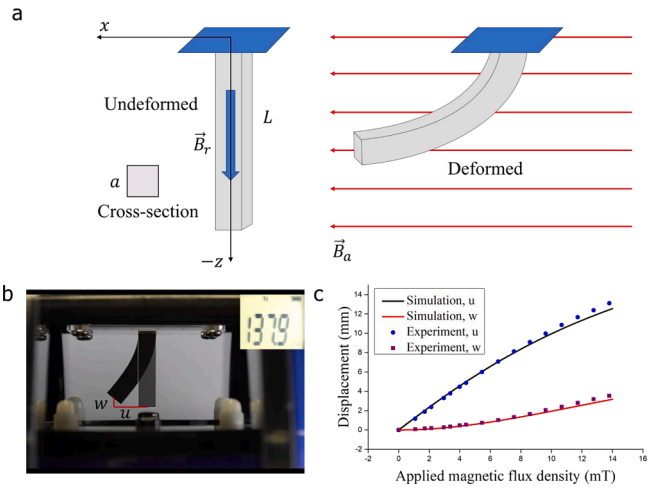

Fig. 4. (a) Schematic of the vertically placed magnetized straight rod applied a horizontal applied magnetic flux density $\vec{B}_a$. The rod length and side length of cross-section are prescribed as $L = 30\,\text{mm}$ and $a = 7\,\text{mm}$. The residual magnetic flux density of the rod $\vec{B}_r$ is along the axis of the rod, and when the rod is subjected to the applied magnetic field, the rod will bend in the direction of the magnetic field. (b) The Configuration before deformation $\left|\vec{B}_a\right| = 0$ mT an d after deformation $\left|\vec{B}_a\right| = 13.79\,\text{mT}$. The displacements of the tip of the rod are expressed in u and w. (c) magnitudes of the tip displacements with the different applied magnetic flux density of the experimental and simulation results. Black line is the simulation results of the horizontal displacement u, red line is the simulation results of the vertical displacement w, blue dot is the experimental results of the horizontal displacement u, and purple dot is the experimental results of the vertical displacement w.

stiffness of the material under magnetization. To investigate the effect of dipole–dipole interactions, we measure the initial shear modulus of the hard-magnetic soft materials before and after magnetization. The initial shear modulus of the material after magnetization is measured as $\mu_e = 38.07 \pm 0.37$ kPa, and the modulus before magnetization is measured as $\mu_e' = 36.58 \pm 0.96$ kPa. The results proves that the dipole–dipole interactions indeed affect the stretch stiffness of the material but is not large. Therefore, we assume the initial shear modulus of the material after magnetization μ_e is the shear modulus used in the implement. It should be noted this is a simplification, because the effect of dipole–dipole interactions is anisotropy and don't obey the Neo-Hookean model.

In addition, the residual magnetic flux density of the material should be measured. We prepare an axially magnetized straight rod with a square cross-section and measure its surface magnetic flux density $\left|\vec{B}_{surface}\right|$ above the center of the top surface by TM5100 Gaussmeter (Tunkia Co., Ltd). We assume the material under magnetization is an uniformly magnetized body, and the relation between residual magnetic flux density and surface magnetic flux density can be derived by volume integration as

$$\left|\vec{B}_r\right| = \frac{\pi\left|\vec{B}_{surface}\right|}{\left[\arctan\left(\frac{a^2}{2d\sqrt{2a^2+4d^2}}\right) - \arctan\left(\frac{a^2}{2(d+L)\sqrt{2a^2+4(d+L)^2}}\right)\right]}, \tag{60}$$

where a is the side length of the cross-section, L is the length of the rod, and d is the distance between measure point and the top surface. The shape of the rod is the same as the rod in Section 4.3, where $a = 7$mm, $L = 30$mm, and $d = 0.1$ mm. The fabricated hard-magnetic soft rod (Section 4.3 and Section 4.4) possesses the residual magnetic flux density $\left|\vec{B}_r\right| = 78.52 \pm 0.74\,\text{mT}$. We assume the shape of sample will not affect the residual magnetic flux density.

We generate the applied magnetic field by the device shown in Fig. 2 (c). When we put a current into the Helmholtz coil, a homogeneous magnetic field will be generated within the coil. And the amplitude of the magnetic field can be controlled by the direct-current power source. The amplitude of the applied magnetic flux density is measured by the TM5100 Gaussmeter (Tunkia Co., Ltd).

4.2. Deformation of a straight soft rod subjected to fixed-end load

Consider a straight rod of length $L = 100\,\text{mm}$ aligned with the x-axis. It is subjected to a concentrated force F in the negative z-direction on its free end, as shown in Fig. 3(a). The cross-section of the rod is a square with a side length $a = 20\,\text{mm}$, and the reasonable factor $k_1 = k_2 = \frac{5}{6}$. The initial shear modulus of the rod is 100 kPa. In this subsection, we compare the simulation results obtained by different computation methods. Therefore, we do not apply the modulus of the material applied in the experiments, in addition, the weight of the rod is ignored in the simulations in the subsection. The magnitude of the tip displacement in x-direction and z-direction are donated by δ_x and δ_z, respectively. In this case, the rod will produce three deformation modes: bending, shearing, and stretching. The total displacement of the rod subjected to a large concentrated force $F = 2\,\text{N}$ is shown in Fig. 3(b).

Fig. 3(c) and (d) show the magnitude of the tip displacement of the results obtained with (i) three-dimensional soild finite element model (14936 tetraheron elements), (ii) the present HMS rod model that considers the nonlinear stress–strain relation and the areal change of the cross-section with 3 elements (quadratic elements) and (iii) the classic geometrically exact beam (C-GEB) model (Simo and Vu-Quoc, 1986) with rigid cross-section assumption and linear stress–strain relation with 3 elements (quadratic elements). The rusults obatined with our model with few elements show great agreement with the rusults obatined with three-dimensional soild finite element model. Therefore, we conclude that our model is efficient and accurate for predicting the deformation of soft beams when there are extra load other than the magnetic field load.

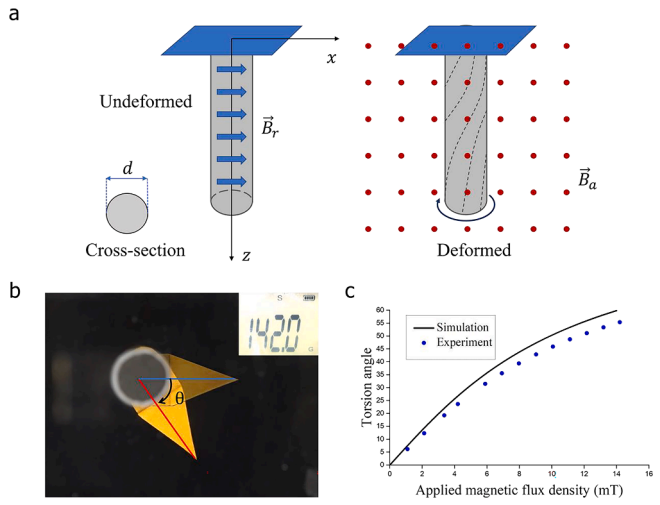

Fig. 5. (a) Schematic of the vertically placed horizontally magnetized cylindrical rod applied an orthogonal applied magnetic flux density $\vec{B}_a$. The rod length and diameter of cross-section are prescribed as $L = 30\,\text{mm}$ and $d = 7\,\text{mm}$. The residual magnetic flux density of the rod $\vec{B}_r$ is perpendicular to the applied magnetic flux density, and when the rod is applied the applied magnetic field, the rod will twist. (b) The Configuration before deformation (blue line) $\left|\vec{B}_a\right| = 0\,\text{mT}$ and after deformation (red line) $\left|\vec{B}_a\right| = 14.20\,\text{mT}$. The torsion angle of the rod are expressed in θ. (c) magnitudes of the torsion angle with the different applied magnetic flux density of the experimental and simulation results. Black line is the simulation results of the torsion angle θ, and blue dot is the experimental results of the torsion angle θ.

4.3. Bending of a hard-magnetic soft rod under a constant field

In this subsection, we consider an axially magnetized straight rod aligned with the negative z-axis applied a x-direction applied magnetic flux density $\vec{B}_a$, as shown in Fig. 4(a). The rod is subjected to gravity and the applied magnetic field, causing it to bend to follow the direction of the magnetic field.

To validate the numerical predictions for the bending of the hard-magnetic soft rod experimentally, we prepared a straight rod of length $L = 30\,\text{mm}$. The cross-section of the rod is a square of side length $a = 7\,\text{mm}$. Fig. 4(b) shows the rod configuration before and after deformation in the experiment, and we measure the displacements of the tip of the rod u and w by the photos of the experiment.

In the experiment, the applied magnetic flux density slowly increases from 0 to 14 mT, and Fig. 4(c) shows the experiment and simulation results of the tip displacements. Surprisingly, the experimental results are in high agreement with the results predicted by the simulation. It's worth mentioning that we calculated such good results with only 5 elements. For these reasons, we conclude that our model is very accurate and efficient for predicting the bending and shear deformation of the HMS rod.

4.4. Torsion of a hard-magnetic soft rod under a constant field

To further validate our model for the case of the torsion of the HMS rod, a horizontally magnetized cylindrical hard-magnetic soft rod of length $L = 30\,\text{mm}$ and diameter $d = 7\,\text{mm}$ was prepared, and we applied a y-direction applied magnetic flux density $\vec{B}_a$ orthogonal to the x-dirction residual magnetic flux density of the rod $\vec{B}_r$ to twist the rod shown as Fig. 5(a). In this case, the gravity play an insignificant role in the deformation of the beam. Therefore we can ignore it. We adhered a triangular piece of yellow paper on the tip of the rod, and slowly increase the applied magnetic flux density from 0 to 14 mT as shown in Fig. 5(b). The torsion angle θ of tip of the rod can be measured by the directions of the paper piece before and after deformation. During the simulation, five elements are used to calculate this case.

Fig. 5(c) shows the torsion angle of tip of the rod enhances with the increase of the applied magnetic flux density, and the simulation results (black line) fit the experimental results (blue dot) well, the error between simulation and experiment is within 10%. Particularly, the simulation results (torsion angle) is generally larger than the experimental results. In our opinion, the fact that the residual magnetic flux density of the rod did not point perfectly along the x-axis caused this discrepancy. Due to the absence of a flat-sided face to serve as a direction indicator, cylindrical rods with horizontal magnetization are more challenging to align in experiments than square or axially magnetized rods. When the angle between the residual magnetic flux density and the applied magnetic flux density is slightly less than 90°, the torsion angle obtained in the experiment will be undersized. In addition, the torsion angle measurement will also introduce some errors.

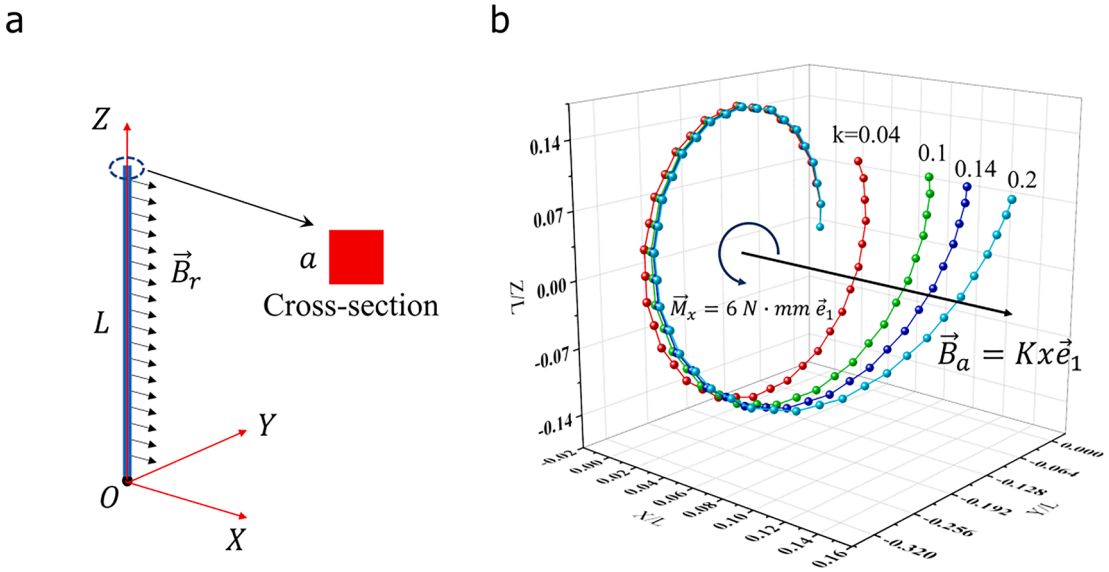

Fig. 6. (a) The undeformed configuration of the horizontally magnetized hard-magnetic soft rod fixed at one end. The rod length and side length of cross-section are prescribed as $L = 100.0\,\text{mm}$ and $a = 10.0\,\text{mm}$. The residual magnetic flux density of the rod $\vec{B}_r$ is aligned with x-direction (b) The deformed shapes of the rod with the different gradient of the applied magnetic flux density $K = k\,\text{mT/mm}$.

4.5. 3D deformation of a straight soft rod under constant gradient field

To demonstrate our model's ability to predict 3D deformation of the hard-magnetic soft rod, a horizontally magnetized hard-magnetic soft rod shown in Fig. 6(a) is considered. The rod is aligned with the z-axis and one end is fixed at the origin, and its residual magnetic flux density along the x-direction. The length of rod is $L = 100.0$ mm, and the cross-section of rod is a square with a side length of $a = 10.0$ mm. The initial shear modulus of the rod is 40 kPa. Similar to the Section 4.2, the weight of the rod is ignored. The HMS rod possesses the residual magnetic flux density of $\left|\vec{B}_r\right| = 100$ mT. In this case, a bending moment (not caused by the applied magnetic field) in the x-direction of $\left|\vec{M}_x\right| = 6$ N·mm is applied at the free end of the rod firstly, and then a constant gradient magnetic flux density $\vec{B}_a = Kx\vec{e}_1$ is applied, where $K = k$ mT/mm is the gradient of the applied magnetic flux density. Fig. 6(b) shows the deformed shapes of the rod with the different amplitudes of the gradient of the applied magnetic flux density k.

5. Conclusions

In this work, we have formulated a mechanics model considering cross-section deformation for the HMS rod under three-dimensional large deformation. In our model, we assume a simple cross-section deformation mode, and then define the deformation gradient of the material by the parameters in the centroid-based description, as shown in Eq. (14). The incompressible neo-Hookean model is used to describe the soft material, and the constitutive equations of the soft rod Eq. (22) is obtained by reducing the strain energy into the centroid-based description. The HMS material is assumed to be ideal HMS material, and the equilibrium equations of the HMS rod are given by Eq. (34), Eq. (35), and Eq. (36). It is worth mentioning that our model include the gradient magnetic field. In Section 3, the finite element formulation and the matrix equations of the problem are presented.

To verify the accuracy and efficacy of our model, four simulation examples and two experiments about the HMS beam are presented. In the first example (Section 4.2), we study the deformation of a straight soft rod subject to fixed-end load, and compare the differences between the results obtained with 3D soild finite element model, our HMS rod model, and the classic geometrically exact beam model. The performance of the HMS model is far better than the classic geometrically exact beam model. In the second and third examples (Section 4.3 and 4.4), the bending and torsion of the HMS rod under a constant field are studied. All simulation results calculated by using 3 or 5 elements are compared with the experimental results, and the error is within 10%. Finally, we discuss the 3D deformation of the HMS rod under constant gradient field.

Although our model performs excellently in predicting the deformation of the HMS rod, some limitations still exist and should be discussed: (1) The constitutive model of the HMS material used in this work give a linear relation between the applied magnetic field and the magnetic flux density. This mean our model is appropriate when applied magnetic field is not large. In addition, in this constitutive model, the dipole–dipole interactions are not considered. Our experiments show the error induced by ignoring this effect is small, however, when the mass fraction of magnetic particles increases, this effect cannot be ignored. Incorporating the dipole–dipole interactions and the nonlinear constitutive law into the rod model is an important task. (2) The distribution of the applied magnetic flux density in our model is a simplification, and the real distribution should be calculated by 3D electromagnetic finite element simulations of the surrounding environment. Including the electromagnetic field in the environment around the rod into our model is a herculean and interesting direction of our future work. (3) The deformation and shape of the rod in our model are also limited. The cross-section deformation is assumed to be dominated by the deformation caused by tension or compression. Therefore the model might not be appropriate for the thick rod with large bending. And the torsion-warping deformation is ignored in this model, which will cause a higher torsion stiffness with the noncircular cross-section than the actual situation. Considering the cross-section deformation caused by large bending, torsion, and shear is an unavoidable challenge in our future work. In addition, the curved rod also should be studied.

Overall, this model obtained in this paper can help the researchers to design and optimize the shape of the HMS rod used in the soft robots, mechanical sensors, and so on. Researchers can develop a more complex structure model of HMS material based on this work.

Declaration of Competing Interest

The authors declare that they have no known competing financial interests or personal relationships that could have appeared to influence the work reported in this paper.

Data availability

Data will be made available on request.

Acknowledgements

The authors would like to acknowledge the funding support from the National Natural Science Foundation of China (grant no. 12072143, grant no. 12172160), the Stable Support Plan Program of Shenzhen Natural Science Fund (grant no. 20200925155345003), and the Science, Technology and Innovation Commission of Shenzhen Municipality (grant no. ZDSYS20210623092005017).

Appendix A

Before building the constitutive equations, the appropriate strain measures conjugate to the resultant force and moment should be defined. Simo (Simo, 1985) proved $\vec{\Gamma}$ and $\vec{\mathrm{K}}$ conjugate to $\vec{N}$ and $\vec{M}$ with rigid cross-section assumption. In this section, we proved that $\vec{\Gamma}$ and $\vec{\mathrm{K}}$ also conjugate to $\vec{N}$ and $\vec{M}$ with our kinematical assumptions. In this discussion, we consider that all variables are functions of time τ.

The first Piola-Kirchhoff stress tensor $\overline{P}(X_1, X_2, S, \tau)$ can be defined as

$$\overline{P} = \vec{T}_1 \otimes \vec{E}_1 + \vec{T}_2 \otimes \vec{E}_2 + \vec{T}_3 \otimes \vec{E}_3. \tag{61}$$

Therefore, $\vec{n}$ and $\vec{m}$ can be easily expressed by

$$\begin{aligned} \vec{n} &= \iint_{A_0} \overline{P}\vec{E}_3 dX_1 dX_2 = \iint_{A_0} \vec{T}_3 dX_1 dX_2, \\ \vec{m} &= \iint_{A_0} (\vec{x} - \vec{\varphi}) \times \overline{P}\vec{E}_3 dX_1 dX_2 = \iint_{A_0} (\vec{x} - \vec{\varphi}) \times \vec{T}_3 dX_1 dX_2. \end{aligned} \tag{62}$$

The internal power Θ can be expressed as

$$\Theta = \iiint_{A_0 \times L} \overline{P} : \dot{\overline{F}} dX_1 dX_2 dS. \tag{63}$$

Using Eq. (13), the time derivative of the deformation gradient can be given by

$$\begin{aligned}\dot{\overline{F}} = &\frac{\left(\vec{w} \times \vec{t}_\eta\right) \otimes \vec{E}_\eta}{\sqrt{\lambda}} - \frac{\dot{\lambda}}{2\lambda\sqrt{\lambda}} \vec{t}_\eta \otimes \vec{E}_\eta + \left[\frac{\partial \dot{\vec{\varphi}}}{\partial S} + \dot{\vec{\omega}} \times (\vec{x} - \vec{\varphi})\right] \otimes \vec{E}_3 + \{\vec{\omega} \times [\vec{w} \times (\vec{x} - \vec{\varphi})]\} \otimes \vec{E}_3 \\ &- \left[\frac{\dot{\lambda}_0}{2\lambda_0} \vec{\omega} \times (\vec{x} - \vec{\varphi})\right] \otimes \vec{E}_3,\end{aligned} \tag{64}$$

where $\vec{w}$ is defined by

$$\begin{aligned}&\vec{w} \times \vec{t}_i = \dot{\vec{t}}_i, \\ &\vec{w}^{\wedge} = \left(\frac{\partial}{\partial \tau} \overline{\Lambda}\right) \overline{\Lambda}^T\end{aligned} \tag{65}$$

Thus, it follows that

$$\begin{aligned}\overline{P} : \dot{\overline{F}} = &\frac{\vec{w} \cdot \left(\vec{t}_\eta \times \vec{T}_\eta\right)}{\sqrt{\lambda}} + \frac{\partial \dot{\vec{\varphi}}}{\partial S} \cdot \vec{T}_3 + \dot{\vec{\omega}} \cdot \left[(\vec{x} - \vec{\varphi}) \times \vec{T}_3\right] + \{\vec{\omega} \times [\vec{w} \times (\vec{x} - \vec{\varphi})]\} \cdot \vec{T}_3 \\ &- \frac{\dot{\lambda}}{2\lambda\sqrt{\lambda}} \vec{t}_\eta \cdot \vec{T}_\eta - \left[\frac{\dot{\lambda}_0}{2\lambda_0} \vec{\omega} \times (\vec{x} - \vec{\varphi})\right] \cdot \vec{T}_3.\end{aligned} \tag{66}$$

With the angular momentum balance condition $\frac{\partial \vec{x}}{\partial X_\eta} \times \vec{T}_\eta + \frac{\partial \vec{x}}{\partial S} \times \vec{T}_3 = 0$ and Eq. (10), the first term in Eq. (66) can be given by

$$\begin{aligned}&\frac{\vec{w} \cdot \left(\vec{t}_\eta \times \vec{T}_\eta\right)}{\sqrt{\lambda}} = \vec{w} \cdot \left(\frac{\partial \vec{x}}{\partial X_\eta} \times \vec{T}_\eta\right) = -\vec{w} \cdot \left(\frac{\partial \vec{x}}{\partial S} \times \vec{T}_3\right) \\ &= -\vec{T}_3 \cdot \left\{\vec{w} \times \frac{\partial \vec{\varphi}}{\partial S} + \vec{w} \times \left[\vec{\omega} \times (\vec{x} - \vec{\varphi})\right]\right\}.\end{aligned} \tag{67}$$

For the majority of beams, the normal stresses between longitudinal fibers of rod are small, such that

$$\vec{t}_1 \cdot \vec{T}_1 \approx \vec{t}_2 \cdot \vec{T}_2 \approx 0. \tag{68}$$

The second and last terms in Eq. (66) can be expressed as

$$\begin{aligned}&\frac{\partial \dot{\vec{\varphi}}}{\partial S} \cdot \vec{T}_3 - \left[\frac{\dot{\lambda}_0}{2\lambda_0} \vec{\omega} \times (\vec{x} - \vec{\varphi})\right] \cdot \vec{T}_3 = \frac{\partial \dot{\vec{\varphi}}}{\partial S} \cdot \left\{\overline{1} - \frac{\vec{t}_3 \otimes [\vec{\omega} \times (\vec{x} - \vec{\varphi})]}{2\lambda_0}\right\} \vec{T}_3 \\ &= \frac{\partial \dot{\vec{\varphi}}}{\partial S} \cdot [\overline{1} - O(\varepsilon)] \vec{T}_3 \approx \frac{\partial \dot{\vec{\varphi}}}{\partial S} \cdot \vec{T}_3.\end{aligned} \tag{69}$$

Substituting Eq. (66), Eq. (67), Eq. (68), and Eq. (69) into Eq. (63), the internal power Θ can be expressed as

$$\begin{aligned}\Theta = &\iiint_{A_0 \times L} \left\{\left(\frac{\partial \dot{\vec{\varphi}}}{\partial S} - \vec{w} \times \frac{\partial \vec{\varphi}}{\partial S}\right) \cdot \vec{T}_3 + \left\{\vec{\omega} \times [\vec{w} \times (\vec{x} - \vec{\varphi})] - \vec{w} \times \left[\vec{\omega} \times (\vec{x} - \vec{\varphi})\right]\right\} \cdot \vec{T}_3 + \dot{\vec{\omega}} \cdot \left[(\vec{x} - \vec{\varphi}) \times \vec{T}_3\right]\right\} dX_1 dX_2 dS \\ = &\iiint_{A_0 \times L} \left\{\left(\frac{\partial \dot{\vec{\varphi}}}{\partial S} - \vec{w} \times \frac{\partial \vec{\varphi}}{\partial S}\right) \cdot \vec{T}_3 + [(\vec{\omega} \times \vec{w}) \times (\vec{x} - \vec{\varphi})] \cdot \vec{T}_3 + \dot{\vec{\omega}} \cdot \left[(\vec{x} - \vec{\varphi}) \times \vec{T}_3\right]\right\} dX_1 dX_2 dS \\ = &\iiint_{A_0 \times L} \left\{\left(\frac{\partial \dot{\vec{\varphi}}}{\partial S} - \vec{w} \times \frac{\partial \vec{\varphi}}{\partial S}\right) \cdot \vec{T}_3 + (\vec{\omega} \times \vec{w}) \cdot \left[(\vec{x} - \vec{\varphi}) \times \vec{T}_3\right] + \dot{\vec{\omega}} \cdot \left[(\vec{x} - \vec{\varphi}) \times \vec{T}_3\right]\right\} dX_1 dX_2 dS \\ = &\int_L \left(\frac{\partial \dot{\vec{\varphi}}}{\partial S} - \vec{w} \times \frac{\partial \vec{\varphi}}{\partial S}\right) \cdot \vec{n} + \left(\dot{\vec{\omega}} - \vec{w} \times \vec{\omega}\right) \cdot \vec{m} dS \\ = &\int_L \left[\frac{\partial}{\partial \tau}\left(\overline{\Lambda}\overline{\Gamma} + \vec{t}_3\right) - \vec{w}^{\wedge} \overline{\Lambda}\left(\overline{\Gamma} + \vec{E}_3\right)\right] \cdot \left(\overline{\Lambda}\vec{N}\right) + \left[\frac{\partial}{\partial \tau}\left(\overline{\Lambda}\overline{\mathrm{K}}\right) - \vec{w}^{\wedge} \overline{\Lambda}\overline{\mathrm{K}}\right] \cdot \left(\overline{\Lambda}\vec{M}\right) dS \\ = &\int_L \left[\dot{\overline{\Lambda}}\left(\overline{\Gamma} + \vec{E}_3\right) + \overline{\Lambda}\dot{\overline{\Gamma}} - \dot{\overline{\Lambda}}\overline{\Lambda}^T \overline{\Lambda}\left(\overline{\Gamma} + \vec{E}_3\right)\right] \cdot \left(\overline{\Lambda}\vec{N}\right) + \left[\dot{\overline{\Lambda}}\overline{\mathrm{K}} + \overline{\Lambda}\dot{\overline{\mathrm{K}}} - \dot{\overline{\Lambda}}\overline{\Lambda}^T \overline{\Lambda}\overline{\mathrm{K}}\right] \cdot \left(\overline{\Lambda}\vec{M}\right) dS \\ = &\int_L \left[(\overline{\Lambda}\dot{\overline{\Gamma}}) \cdot \left(\overline{\Lambda}\vec{N}\right) + \left(\overline{\Lambda}\dot{\overline{\mathrm{K}}}\right) \cdot \left(\overline{\Lambda}\vec{M}\right)\right] dS = \int_L \left(\vec{N} \cdot \dot{\overline{\Gamma}} + \vec{M} \cdot \dot{\overline{\mathrm{K}}}\right) dS.\end{aligned} \tag{70}$$

Therefore, in our model, $\vec{\Gamma}$ and $\vec{K}$ conjugate to $\vec{N}$ and $\vec{M}$.

Appendix B. Supplementary data

Supplementary data to this article can be found online at https://doi.org/10.1016/j.ijsolstr.2023.112344.

References

Bathe, K.-.-J. (Ed.), 2014. Finite element procedures, 2nd ed. K.J. Bathe, Watertown, MA.

Cao, X., Zhang, M., Zhang, Z., Xu, Y., Xiao, Y., Li, T., 2019. Review of soft linear actuator and the design of a dielectric elastomer linear actuator. Acta Mech. Solida Sin. 32, 566–579. https://doi.org/10.1007/s10338-019-00112-8.

Chen, W., Wang, L., 2020. Theoretical modeling and exact solution for extreme bending deformation of hard-magnetic soft beams. J. Appl. Mech. 87, 041002. https://doi.org/10.1115/1.4045716.

Chen, W., Yan, Z., Wang, L., 2020. Complex transformations of hard-magnetic soft beams by designing residual magnetic flux density. Soft Matter. 16, 6379–6388. https://doi.org/10.1039/C9SM02529D.

Chen, W., Yan, Z., Wang, L., 2020. On mechanics of functionally graded hard-magnetic soft beams. Int. J. Eng. Sci. 157, 103391. https://doi.org/10.1016/j.ijengsci.2020.103391.

Chen, W., Wang, L., Yan, Z., Luo, B., 2021. Three-dimensional large-deformation model of hard-magnetic soft beams. Compos. Struct. 266, 113822. https://doi.org/10.1016/j.compstruct.2021.113822.

Chen, W., Wang, L., Yan, Z., 2023. On the dynamics of curved magnetoactive soft beams. Int. J. Eng. Sci. 183, 103792. https://doi.org/10.1016/j.ijengsci.2022.103792.

Chen, Y., Zhao, X., Li, Y., Jin, Z.-Y., Yang, Y., Yang, M.-B., Yin, B., 2021. Light- and magnetic-responsive synergy controlled reconfiguration of polymer nanocomposites with shape memory assisted self-healing performance for soft robotics. J. Mater. Chem. C 9, 5515–5527. https://doi.org/10.1039/D1TC00468A.

Chung, H., Parsons, A.M., Zheng, L., 2021. Magnetically controlled soft robotics utilizing elastomers and gels in actuation: a review. Adv. Intell. Syst. 3, 2000186. https://doi.org/10.1002/aisy.202000186.

Crisfield, M.A., Jelenić, G., 1999. Objectivity of strain measures in the geometrically exact three-dimensional beam theory and its finite-element implementation. Proc. R. Soc. Lond. Ser. Math. Phys. Eng. Sci. 455, 1125–1147. https://doi.org/10.1098/rspa.1999.0352.

Dadgar-Rad, F., Hossain, M., 2022. Finite deformation analysis of hard-magnetic soft materials based on micropolar continuum theory. Int. J. Solids Struct. 251, 111747. https://doi.org/10.1016/j.ijsolstr.2022.111747.

Dadgar-Rad, F., Hossain, M., 2022. Large viscoelastic deformation of hard-magnetic soft beams. Extreme Mech. Lett. 54, 101773. https://doi.org/10.1016/j.eml.2022.101773.

Dasambiagio, E.R., Pimenta, P.M., Campello, E.M.B., 2009. A finite strain rod model that incorporates general cross section deformation and its implementation by the Finite Element Method.

Dehrouyeh-Semnani, A.M., 2021. On bifurcation behavior of hard magnetic soft cantilevers. Int. J. Non-Linear Mech. 134, 103746. https://doi.org/10.1016/j.ijnonlinmec.2021.103746.

Diller, E., Zhuang, J., Zhan Lum, G., Edwards, M.R., Sitti, M., 2014. Continuously distributed magnetization profile for millimeter-scale elastomeric undulatory swimming. Appl. Phys. Lett. 104, 174101. https://doi.org/10.1063/1.4874306.

Du, X., Cui, H., Xu, T., Huang, C., Wang, Y., Zhao, Q., Xu, Y., Wu, X., 2020. Reconfiguration, camouflage, and color-shifting for bioinspired adaptive hydrogel-based millirobots. Adv. Funct. Mater. 30, 1909202. https://doi.org/10.1002/adfm.201909202.

Finney, R.H., 2012. Finite element analysis. In: Eng. Rubber, 3rd ed., Carl Hanser Verlag GmbH & Co. KG, München, pp. 295–343. https://doi.org/10.3139/9783446428713.009.

Furusawa, M., Maeda, K., Azukizawa, S., Shinoda, H., Tsumori, F., 2019. Bio-mimic motion of elastic material dispersed with hard-magnetic particles. J. Photopolym. Sci. Technol. 32, 309–313. https://doi.org/10.2494/photopolymer.32.309.

Garcia-Gonzalez, D., Ter-Yesayants, T., Moreno-Mateos, M.A., Lopez-Donaire, M.L., 2023. Hard-magnetic phenomena enable autonomous self-healing elastomers. Compos. Part B Eng. 248, 110357. https://doi.org/10.1016/j.compositesb.2022.110357.

Hines, L., Petersen, K., Lum, G.Z., Sitti, M., 2017. Soft actuators for small-scale robotics. Adv. Mater. 29, 1603483. https://doi.org/10.1002/adma.201603483.

Joo, H., Lee, Y., Kim, J., Yoo, J.-S., Yoo, S., Kim, S., Arya, A.K., Kim, S., Choi, S.H., Lu, N., Lee, H.S., Kim, S., Lee, S.-T., Kim, D.-H., 2021. Soft implantable drug delivery device integrated wirelessly with wearable devices to treat fatal seizures. Sci. Adv. 7, eabd4639. https://doi.org/10.1126/sciadv.abd4639.

Kang, D.J., An, S., Yarin, A.L., Anand, S., 2019. Programmable soft robotics based on nano-textured thermo-responsive actuators. Nanoscale 11, 2065–2070. https://doi.org/10.1039/C8NR08215D.

Kim, Y., Yuk, H., Zhao, R., Chester, S.A., Zhao, X., 2018. Printing ferromagnetic domains for untethered fast-transforming soft materials. Nature 558, 274–279. https://doi.org/10.1038/s41586-018-0185-0.

Kim, Y., Parada, G.A., Liu, S., Zhao, X., 2019. Ferromagnetic soft continuum robots. Sci. Robot. 4, eaax7329. https://doi.org/10.1126/scirobotics.aax7329.

Kim, Y., Zhao, X., 2022. Magnetic soft materials and robots. Chem. Rev. 122, 5317–5364. https://doi.org/10.1021/acs.chemrev.1c00481.

Klinkel, S., Govindjee, S., 2003. Anisotropic bending-torsion coupling for warping in a non-linear beam. Comput. Mech. 31, 78–87. https://doi.org/10.1007/s00466-002-0395-y.

Li, X., Yu, W., Baghaee, M., Cao, C., Chen, D., Liu, J.u., Yuan, H., 2022. Geometrically exact finite element formulation for tendon-driven continuum robots. Acta Mech. Solida Sin. 35 (4), 552–570.

Lum, G.Z., Ye, Z., Dong, X., Marvi, H., Erin, O., Hu, W., Sitti, M., 2016. Shape-programmable magnetic soft matter. Proc. Natl. Acad. Sci. 113 https://doi.org/10.1073/pnas.1608193113.

Ma, H., Zhou, J., 2023. Modeling, characterization, and application of soft bellows-type pneumatic actuators for bionic locomotion. Acta Mech. Solida Sin. 36 (1), 1–12.

Mukherjee, D., Danas, K., 2022. A unified dual modeling framework for soft and hard magnetorheological elastomers. Int. J. Solids Struct. 257, 111513. https://doi.org/10.1016/j.ijsolstr.2022.111513.

Mukherjee, D., Rambausek, M., Danas, K., 2021. An explicit dissipative model for isotropic hard magnetorheological elastomers. J. Mech. Phys. Solids 151, 104361. https://doi.org/10.1016/j.jmps.2021.104361.

Petrov, E., Géradin, M., 1998. Finite element theory for curved and twisted beams based on exact solutions for three-dimensional solids Part 1: Beam concept and geometrically exact nonlinear formulation. Comput. Methods Appl. Mech. Eng. 165, 43–92. https://doi.org/10.1016/S0045-7825(98)00061-9.

Petrov, E., Géradin, M., 1998. Finite element theory for curved and twisted beams based on exact solutions for three-dimensional solids Part 2: Anisotropic and advanced beam models. Comput. Methods Appl. Mech. Eng. 165, 93–127. https://doi.org/10.1016/S0045-7825(98)00060-7.

Pimenta, P.M., Campello, E.M.B., 2003. A fully nonlinear multi-parameter rod model incorporating general cross-sectional in-plane changes and out-of-plane warping. Lat. Am. J. Solids Struct.

Rajan, A., Arockiarajan, A., 2021. Bending of hard-magnetic soft beams: a finite elasticity approach with anticlastic bending. Eur. J. Mech. – A Solids 90, 104374. https://doi.org/10.1016/j.euromechsol.2021.104374.

Rong, J., Wu, Z., Liu, C., Brüls, O., 2020. Geometrically exact thin-walled beam including warping formulated on the special Euclidean group S E (3). Comput. Methods Appl. Mech. Eng. 369, 113062. https://doi.org/10.1016/j.cma.2020.113062.

Sano, T.G., Pezzulla, M., Reis, P.M., 2022. A Kirchhoff-like theory for hard magnetic rods under geometrically nonlinear deformation in three dimensions. J. Mech. Phys. Solids 160, 104739. https://doi.org/10.1016/j.jmps.2021.104739.

Simo, J.C., 1985. A finite strain beam formulation. The three-dimensional dynamic problem. Part I. Comput. Methods Appl. Mech. Eng. 49, 55–70 https://doi.org/10/cvb8rf.

Simo, J.C., Vu-Quoc, L., 1986. A three-dimensional finite-strain rod model. Part II: computational aspects. Comput. Methods Appl. Mech. Eng. 58, 79–116 https://doi.org/10/b8wd4z.

Simo, J.C., Vu-Quoc, L., 1991. A Geometrically-exact rod model incorporating shear and torsion-warping deformation. Int. J. Solids Struct. 27, 371–393. https://doi.org/10.1016/0020-7683(91)90089-X.

Sitti, M., Wiersma, D.S., 2020. Pros and cons: magnetic versus optical microrobots. Adv. Mater. 32, 1906766. https://doi.org/10.1002/adma.201906766.

Sokolov, I., Krylov, S., Harari, I., 2015. Extension of non-linear beam models with deformable cross sections. Comput. Mech. 56, 999–1021. https://doi.org/10.1007/s00466-015-1215-5.

Stepanov, G.V., Chertovich, A.V., Kramarenko, E.Y., 2012. Magnetorheological and deformation properties of magnetically controlled elastomers with hard magnetic filler. J. Magn. Magn. Mater. 324, 3448–3451. https://doi.org/10.1016/j.jmmm.2012.02.062.

Wang, L., Kim, Y., Guo, C.F., Zhao, X., 2020. Hard-magnetic elastica. J. Mech. Phys. Solids 142, 104045. https://doi.org/10.1016/j.jmps.2020.104045.

Wang, W., Yao, Z., Chen, J.C., Fang, J., 2004. Composite elastic magnet films with hard magnetic feature. J. Micromech. Microeng. 14, 1321–1327. https://doi.org/10.1088/0960-1317/14/10/005.

Wu, Y., Zhang, S., Yang, Y., Li, Z., Wei, Y., Ji, Y., 2022. Locally controllable magnetic soft actuators with reprogrammable contraction-derived motions. Sci. Adv. 8, eabo6021. https://doi.org/10.1126/sciadv.abo6021.

Xu, T., Zhang, J., Salehizadeh, M., Onaizah, O., Diller, E., 2019. Millimeter-scale flexible robots with programmable three-dimensional magnetization and motions. Sci. Robot. 4, eaav4494. https://doi.org/10.1126/scirobotics.aav4494.

Yan, D., Abbasi, A., Reis, P.M., 2021. A comprehensive framework for hard-magnetic beams: reduced-order theory, 3D simulations, and experiments. Int. J. Solids Struct. 111319. https://doi.org/10.1016/j.ijsolstr.2021.111319.

Ye, J., Yao, Y.-C., Gao, J.-Y., Chen, S., Zhang, P., Sheng, L., Liu, J., 2022. LM-Jelly: liquid metal enabled biomimetic robotic jellyfish. Soft Robot. 9 (6), 1098–1107.
Yu, W., Li, X., Chen, D., Liu, J., Su, J., Liu, J., Cao, C., Yuan, H., 2022. A minimally designed soft crawling robot for robust locomotion in unstructured pipes. Bioinspir. Biomim. 17, 056001. https://doi.org/10.1088/1748-3190/ac7492.
Yu, Y., Li, J., Solomon, S.A., Min, J., Tu, J., Guo, W., Xu, C., Song, Y., Gao, W., 2022. All-printed soft human-machine interface for robotic physicochemical sensing. Sci. Robot. 7, eabn0495. https://doi.org/10.1126/scirobotics.abn0495.
Zhao, R., Kim, Y., Chester, S.A., Sharma, P., Zhao, X., 2019. Mechanics of hard-magnetic soft materials. J. Mech. Phys. Solids 124, 244–263. https://doi.org/10.1016/j.jmps.2018.10.008.